Journal of Computational Physics **152,** 305–345 (1999)
Article ID jcph.1999.6258, available online at http://www.idealibrary.com on IDEAL®

Dynamic LES of Colliding Vortex Rings Using a 3D Vortex Method

John R. Mansfield,[1] Omar M. Knio,[2] and Charles Meneveau

Department of Mechanical Engineering, The Johns Hopkins University, Baltimore, Maryland 21218-2686
E-mail: knio@jhu.edu

Received August 13, 1998; revised February 9, 1999

A Lagrangian particle method is used to simulate the collision of coaxial vortex rings in three dimensions. The scheme combines a 3D, adaptive, viscous, vortex element method with a dynamic eddy viscosity model of the subfilter scale stresses. The vortex method is based on discretization of the vorticity field into Lagrangian vortex elements and transport of the elements along particle trajectories. The computations incorporate a mesh redistribution algorithm which creates new elements in regions of high strain and locally redistributes the vorticity field into a smaller number of elements when particles tend to cluster. The subfilter scale vorticity model consists of approximating the effect of unresolved vorticity stresses using a gradient–diffusion eddy viscosity model, following the development in Part I (J. R. Mansfield, O. M. Knio, and C. Meneveau, *J. Comput. Phys.* **145**, 693 (1998)). Dynamic implementation of the model relies on determining model coefficients through test-filtering the Lagrangian particle representation of the filtered vorticity field. Computations of ring collisions show that, combined, the mesh redistribution scheme and subfilter scale model result in a robust scheme that can be extended into the late stages of evolution of the flow. In addition, it is shown that the Lagrangian LES scheme captures several experimentally observed features of the ring collisions, including turbulent breakdown into small-scale structures and the generation of small-scale radially propagating vortex rings. © 1999 Academic Press

Key Words: vortex methods; redistribution scheme; Lagrangian simulation; dynamic LES.

1. INTRODUCTION

Particle methods are designed for simulation of high-Reynolds-number flows with concentrated vorticity. They are generally based on discretization of the vorticity field into

---

[1] Current address: Mechanical and Aerospace Engineering, UCLA, Los Angeles, California 90095-1597.
[2] To whom correspondence should be addressed.

0021-9991/99 $30.00

Lagrangian elements and transport of these elements along particle trajectories. The advantages of this approach stem from the Lagrangian discretization which naturally concentrates computational elements into regions of high vorticity, and from the Lagrangian transport which minimizes numerical diffusion.

Due to their natural ability to capture inviscid dynamics of concentrated energetic eddies, vortex methods appear to provide a promising approach to large-eddy-simulation of turbulent flows. The original attempts at Lagrangian LES may be traced to Chorin's hairpin removal algorithms [1–3]. Essentially, these schemes combine a filament-based method with a local mesh redistribution algorithm that removes the filaments' small scales or "hairpins." Hairpin removal schemes have been used in various applications, including boundary layers [4], vortex breakdown [5], and vortex reconnection [6].

In their simplest form, hairpin removal schemes rely on the redistribution scheme to filter out the small scales but maintain the same governing equation for the large scales. Thus, the effect of the unresolved scales is assumed to be accounted for by the hairpin removal process. Recently proposed extensions of the hairpin removal scheme are based on renormalized equations of motion for the large scales [7, 8], including a scale-dependent "dielectric constant" which accounts for the missing scales in the Biot–Savart law [9].

In this paper, we explore a different approach that is applicable to particle-based method as opposed to filament schemes. Specifically, we incorporate the dynamic eddy diffusivity model introduced in our previous effort [10] into a 3D Lagrangian particle scheme. The model accounts for the effect of the subfilter scale (SFS) vorticity stresses on the motion of the resolved scales. The properties of the model were analyzed in [10] in light of *a priori* tests using direct numerical simulations of isotropic turbulence. In particular, these tests showed that the eddy diffusivity model exhibits fair correlation with the SFS torque due to vortex transport, but poor correlation with the SFS torque due to vortex stretching and tilting. Despite this weakness, the tests indicated that the eddy viscosity model for the vorticity transport equation is potentially more realistic than its primitive variable counterpart; a similar conclusion was reached by Winckelmans *et al.* [11]. Numerical experiments were also conducted in [10] in order to explore a particle discretization of the dynamic SFS model. Comparison with spectral collocation results showed that when adequate resolution is provided the particle discretization yields reasonable predictions of both the SFS torques and the dynamic model constant.

Motivated by these results, the present effort focuses on the implementation of the dynamic eddy diffusivity model proposed in [10] in a Lagrangian particle scheme. As outlined in Section 2, the latter is based on discretization of the vorticity field into smooth overlapping vortex elements which move with the local resolved velocity vector. The vorticity carried by the elements changes according to stretching by the resolved strain field, molecular diffusion and the modeled SFS torques. The numerical scheme incorporates a local redistribution algorithm which combines a splitting scheme and a merging scheme. The splitting scheme introduces additional particles in regions of high strain, while the merging scheme eliminates particles in regions where they tend to cluster. Thus, the particle redistribution algorithm mimics the action of hairpin removal in filament-based computations.

In Section 3, the scheme is applied to simulate the collision of coaxial vortex rings in three dimensions. The computational setup resembles the experimental conditions of Lim and Nickels [12], who provide striking dye visualizations of these collisions. In particular, the experimental findings in [12] show that the collision of the two rings results, following a complex cancellation and reconnection process, in the generation of ringlets propagating in the radial direction, away from the center of the collision. However, the experiments also indicate that in some collision events the rings break down into a cloud of turbulence without generating ringlets. This variability and strong dependence on the initial conditions, as well as the development of instabilities, provide a difficult challenge for the computations. Thus, the simulations are used to analyze, qualitatively, possible causes behind the variability between different collision events.

Irrespective of the outcome of the collision, the violent nature of the interaction between the colliding rings provides a stringent test for the computations. The latter show that the present combination of particle redistribution and SFS dynamic model results in a robust scheme that can capture complex flow dynamics with a reasonable number of elements. The present results and conclusions are summarized in Section 4, and are contrasted with previous hairpin removal experiences.

2. FORMULATION AND NUMERICAL SCHEMES

2.1. *Formulation*

The present LES scheme is based on the filtered vorticity transport equation [13],

$$\frac{\partial \tilde{\omega}_i}{\partial t} + \tilde{u}_j \frac{\partial \tilde{\omega}_i}{\partial x_j} = \tilde{\omega}_j \frac{\partial \tilde{u}_i}{\partial x_j} + \nu \nabla^2 \tilde{\omega}_i - \frac{\partial \mathsf{R}_{ij}}{\partial x_j}, \tag{1}$$

where

$$\mathsf{R}_{ij} \equiv (\widetilde{\omega_i u_j} - \tilde{\omega}_i \tilde{u}_j) - (\widetilde{u_i \omega_j} - \tilde{u}_i \tilde{\omega}_j) \tag{2}$$

is the subfilter-scale (SFS) vorticity stress, which accounts for the effect of unresolved velocity and vorticity fluctuations. Tildes are used to denote spatially filtered quantities. In order to close the filtered vorticity transport equation, one must provide a model for the vorticity stress, R, or alternatively for its divergence, $\partial \mathsf{R}_{ij}/\partial x_j$. Following our efforts in [10], we focus on the eddy diffusivity model [11, 13]

$$\nabla \cdot \mathsf{R} \simeq g \equiv -\nabla \cdot (\nu_{\mathrm{T}} \nabla \tilde{\omega}), \tag{3}$$

where

$$\nu_{\mathrm{T}} = C_r^2 \Delta^2 |\tilde{\mathsf{S}}| \tag{4}$$

is the eddy diffusivity. In Eq. (4), Δ is the filter size, $|\tilde{\mathsf{S}}| \equiv \sqrt{2\tilde{\mathsf{S}}_{mn}\tilde{\mathsf{S}}_{mn}}$ is the modulus of the filtered strain-rate tensor, and C_r is a model constant. As discussed below, the filter size Δ is related to the core size of the Lagrangian vortex elements used to represent the vorticity field, while the model constant is determined dynamically in the calculations based on multiple filtering operations.

2.2. *Numerical Scheme*

The present Lagrangian LES scheme is based on a three-dimensional vortex element method. The method is based on discretization of the vorticity field into desingularized elements, according to [14, 15],

$$\boldsymbol{\omega}^{\mathrm{N}}(\boldsymbol{x}, t) = \sum_{i=1}^{N} \zeta_i(t)\, dV_i\, f_\delta(\boldsymbol{x} - \boldsymbol{X}_i(t)), \tag{5}$$

where N is the total number of elements, $\boldsymbol{X}_i$, ζ_i, and dV_i respectively denote the position, strength and volume of the ith element,

$$f_\delta(\boldsymbol{x}) \equiv \frac{1}{\delta^3} f\left(\frac{|\boldsymbol{x}|}{\delta}\right) \tag{6}$$

is a spherical rapidly decaying core function, and δ is the core radius. The vortex elements are assumed to have overlapping cores and the smoothing function f is assumed to satisfy some moment conditions [15, 16] which govern the convergence of the scheme.

For an unbounded domain with no internal boundaries, where the fluid at ∞ is at rest, the velocity field induced by the above vorticity distribution (5) is given by the desingularized Biot–Savart law [15],

$$\boldsymbol{u}(\boldsymbol{x}) = -\frac{1}{4\pi} \sum_{i=1}^{N} \frac{(\boldsymbol{x} - \boldsymbol{X}_i) \times \boldsymbol{\zeta}_i}{|\boldsymbol{x} - \boldsymbol{X}_i|^3}\, dV_i \kappa_\delta(\boldsymbol{x} - \boldsymbol{X}_i), \tag{7}$$

where

$$\kappa_\delta(\boldsymbol{x}) \equiv \kappa\left(\frac{|\boldsymbol{x}|}{\delta}\right); \; \kappa(r) = 4\pi \int_0^r \xi^2 f(\xi)\, d\xi \tag{8}$$

is the velocity smoothing kernel corresponding to f. In all of the computations below, we rely on the third-order Gaussian core function [17]

$$f(r) = \frac{3}{4\pi} \exp(-r^3) \tag{9}$$

with corresponding velocity kernel

$$\kappa(r) = 1 - \exp(-r^3). \tag{10}$$

This choice leads to an essentially second-order accurate discretization [15].

Using the particle representation of the velocity (7) and vorticity (5), we transform the original problem into a system of coupled evolution equations for the particle positions and strengths. We have

$$\frac{d\boldsymbol{X}_i}{dt} = \boldsymbol{u}(\boldsymbol{X}_i) \tag{11}$$

$$\frac{d\boldsymbol{\zeta}_i}{dt} = \boldsymbol{\zeta}_i \cdot \nabla \boldsymbol{u}(\boldsymbol{X}_i) + D[\nu, \boldsymbol{\zeta}](\boldsymbol{X}_i) + D[\nu_{\mathrm{T}}, \boldsymbol{\zeta}](\boldsymbol{X}_i) \tag{12}$$

Here, $D[\nu, \boldsymbol{\zeta}](\boldsymbol{X}_i)$ denotes a particle representation of the diffusion term, while $D[\nu_{\mathrm{T}}, \boldsymbol{\zeta}](\boldsymbol{X}_i)$ is a particle representation of the SFS model. Below, we outline the evaluation of the SFS model but for brevity omit discussion of the diffusion term. However, it is first necessary to recall various filtering operations originally introduced in [10].

2.3. *Filtering*

The present approach is based on associating the resolution limit with the core radius, δ, and considering the vorticity field in (5) to be “particle filtered.” We standardize the definition of size by relating the core size, δ, to the width, Δ, of an equivalent box filter. We introduce the scaling coefficient $c \equiv \Delta/\delta$, and define the (standardized) particle filter [10]:

$$G_\Delta(\boldsymbol{x}) \equiv f_{\Delta/c}(\boldsymbol{x}) = \frac{3}{4\pi}\left(\frac{c}{\Delta}\right)^3 \exp\left[-\left(\frac{c|\boldsymbol{x}|}{\Delta}\right)^3\right]. \tag{13}$$

The constant c is determined by requiring that the particle filter G_Δ have the same characteristic size (i.e., the same energy content $\int |\hat{G}_\Delta(k)|^2 d^3k$) as the spherical box filter,

$$B_\Delta(\boldsymbol{x}) = \begin{cases} \frac{6}{\pi\Delta^3} & \text{if } |\boldsymbol{x}| \leq \Delta/2 \\ 0 & \text{otherwise.} \end{cases} \tag{14}$$

This requirement results in the relationship $\Delta = 2.88243\delta$, i.e., $c = 2.88243$, for the third-order Gaussian.

In addition to the above particle filter, we also introduce a test filter which is assumed to have the same shape as the particle filter but larger width. The test filter is denoted by an overbar and, in the framework of the particle representation, is defined by

$$\overline{q}(\boldsymbol{x}) = \frac{\sum_{i=1}^{N} q(\boldsymbol{X}_i)\exp[-(c|\boldsymbol{x}-\boldsymbol{X}_i|/\Delta')^3]}{\sum_{i=1}^{N}\exp[-(c|\boldsymbol{x}-\boldsymbol{X}_i|/\Delta')^3]}, \tag{15}$$

where q is the quantity being test filtered and Δ' is the width of the test filter.

2.4. *Evaluation of C_r and SFS model*

In order to determine the model constant, the dynamic procedure introduced in Ref. [10] is implemented. (The dynamic scheme in [10] is an adaptation of the dynamic procedure introduced in [18] for the Navier–Stokes equations.) Specifically, it is shown that the “particle-averaged” model constant can be dynamically approximated using [10],

$$C_r^2 = \frac{\sum_{i=1}^{N} \boldsymbol{p}_i \cdot \boldsymbol{q}_i \, dV_i}{\sum_{i=1}^{N} \boldsymbol{q}_i \cdot \boldsymbol{q}_i \, dV_i}, \tag{16}$$

where $\boldsymbol{p}_i \equiv \boldsymbol{p}(\boldsymbol{X}_i)$, $\boldsymbol{q}_i \equiv \boldsymbol{q}(\boldsymbol{X}_i)$,

$$\boldsymbol{p} = \overline{\frac{\tilde{d}\tilde{\boldsymbol{\omega}}}{dt}} - \frac{\bar{\tilde{d}}\bar{\tilde{\boldsymbol{\omega}}}}{dt}, \tag{17}$$

$$\boldsymbol{q} = \Delta^2 \overline{\nabla\cdot(|\tilde{\mathrm{S}}|\nabla\tilde{\boldsymbol{\omega}})} - \Delta'^2 \nabla\cdot(|\bar{\tilde{\mathrm{S}}}|\nabla\bar{\tilde{\boldsymbol{\omega}}}), \tag{18}$$

$\tilde{d}/dt$ represents the time rate of change for an observer moving at $\tilde{\boldsymbol{u}}$, while $\bar{\tilde{d}}/dt$ represents the time rate of change for an observer moving at $\bar{\tilde{\boldsymbol{u}}}$. In the calculations, the filtered Lagrangian derivatives are approximated using backward differences; we use [19]

$$\left[\frac{\tilde{d}\tilde{\boldsymbol{\omega}}}{dt}\right](\boldsymbol{X}_i, t) \approx \frac{\tilde{\boldsymbol{\omega}}(\boldsymbol{X}_i(t), t) - \tilde{\boldsymbol{\omega}}(\boldsymbol{X}_i(t-\Delta t), t-\Delta t)}{\Delta t} \tag{19}$$

and

$$\left[\frac{\bar{\tilde{d}}\bar{\tilde{\boldsymbol{\omega}}}}{dt}\right](\boldsymbol{X}_i, t) \approx \frac{\bar{\tilde{\boldsymbol{\omega}}}(\boldsymbol{X}_i(t), t) - \bar{\tilde{\boldsymbol{\omega}}}(\boldsymbol{X}_i(t) - \Delta t\bar{\tilde{\boldsymbol{u}}}_i(t), t - \Delta t)}{\Delta t} \tag{20}$$

In order to estimate $\boldsymbol{q}$, we rely on the Lagrangian expressions developed by Degond and Mas-Gallic [20], who show that for isotropic spatially varying diffusivity the gradient diffusion operator $D[b,\ f] \equiv \nabla \cdot (b(\boldsymbol{x})\nabla f(\boldsymbol{x}))$ can be approximated as

$$D[b,\ f](\boldsymbol{X}_k) \approx \frac{1}{\delta^2}\sum_l w_l \eta_\delta(\boldsymbol{X}_k - \boldsymbol{X}_l)\mu(\boldsymbol{X}_l, \boldsymbol{X}_k)(f_l - f_k), \tag{21}$$

where $\boldsymbol{X}_l$, w_l, and f_l are the particle positions, volumes and strengths in the Lagrangian representation of f, $\eta_\delta(\boldsymbol{x}) = \delta^{-3}\eta(|\boldsymbol{x}|/\delta)$ is a rapidly decaying smoothing function, and μ is a symmetric kernel which satisfies

$$\mu(\boldsymbol{x}, \boldsymbol{y}) = \mu(\boldsymbol{y}, \boldsymbol{x}) \quad \text{and} \quad \mu(\boldsymbol{x}, \boldsymbol{x}) = b(\boldsymbol{x}). \tag{22}$$

We associate μ with the geometric mean diffusivity; i.e., we set [10]

$$\mu(\boldsymbol{x}, \boldsymbol{y}) = \sqrt{b(\boldsymbol{x})b(\boldsymbol{y})}. \tag{23}$$

Meanwhile, we relate η to the gradient of the core smoothing function using [20]:

$$\eta(r) \equiv g(r) = -\frac{2}{r}\frac{df}{dr}. \tag{24}$$

Using (21), the diffusion term $\nabla \cdot (|\tilde{\mathsf{S}}|\nabla\tilde{\boldsymbol{\omega}})$ is approximated as

$$\nabla \cdot (|\tilde{\mathsf{S}}|\nabla\tilde{\boldsymbol{\omega}})_i \approx \frac{1}{\delta^2}\sum_{j=1}^{N}\sqrt{|\tilde{\mathsf{S}}(\boldsymbol{X}_i)||\tilde{\mathsf{S}}(\boldsymbol{X}_j)|}(\tilde{\boldsymbol{\omega}}(\boldsymbol{X}_j) - \tilde{\boldsymbol{\omega}}(\boldsymbol{X}_i))\, dV_j g_\delta(\boldsymbol{X}_j - \boldsymbol{X}_i), \tag{25}$$

where the filtered strain and vorticity values are obtained from the filtered velocity gradient, $\nabla\tilde{\boldsymbol{u}}$. The latter is obtained by analytically differentiating the desingularized Biot–Savart law and evaluating the resulting expression [21]. Equation (15) is then used to compute a test filtered version of the velocity gradient, which naturally yields the test filtered vorticity $\bar{\tilde{\omega}}$ and strain $\bar{\tilde{\mathsf{S}}}$.

The grid-filtered diffusion term is then test filtered according to

$$\overline{\nabla \cdot (|\tilde{\mathsf{S}}|\nabla\tilde{\boldsymbol{\omega}})}(\boldsymbol{X}_i) = \frac{\sum_{j=1}^{N}\nabla \cdot (|\tilde{\mathsf{S}}|\nabla\tilde{\boldsymbol{\omega}})(\boldsymbol{X}_j)\exp[-(c|\boldsymbol{X}_i - \boldsymbol{X}_j|/\Delta')^3]}{\sum_{j=1}^{N}\exp[-(c|\boldsymbol{X}_i - \boldsymbol{X}_j|/\Delta')^3]}. \tag{26}$$

A similar approach is adopted for the second diffusion in Eq. (18), which involves diffusion of the test filtered vorticity. Specifically, Eq. (21) is once again used in conjunction with the test filtered vorticity $\bar{\tilde{\boldsymbol{\omega}}}$ and strain $\tilde{\mathsf{S}}$; this yields

$$\nabla \cdot (|\bar{\tilde{\mathsf{S}}}|\nabla\bar{\tilde{\boldsymbol{\omega}}})(\boldsymbol{X}_i) \approx \frac{1}{\delta^2}\sum_{j=1}^{N}\sqrt{|\bar{\tilde{\mathsf{S}}}(\boldsymbol{X}_i)||\bar{\tilde{\mathsf{S}}}(\boldsymbol{X}_j)|}(\bar{\tilde{\boldsymbol{\omega}}}(\boldsymbol{X}_j) - \bar{\tilde{\omega}}(\boldsymbol{X}_i))\, dV_j g_\delta(\boldsymbol{X}_j - \boldsymbol{X}_i). \tag{27}$$

The results of Eqs. (26) and (27) are then substituted into Eq. (18), which results in the necessary estimates for $\boldsymbol{q}$. The accuracy of the approximations in Eqs. (25)–(27) was tested in detail in [10] against spectral DNS of isotropic turbulence. The tests in [10] show that when the particle representation is sufficiently resolved the predictions of the particle representation are in good agreement with spectral results.

Once the differences $\boldsymbol{p}$ and $\boldsymbol{q}$ are evaluated for all the Lagrangian particles, the model constant is evaluated from Eq. (16). A priori tests in [10] show that this approach yields realistic values of C_r. Note, however, that the discrete sum in (16) may yield a negative quantity. In this situation, the eddy viscosity is simply set to zero, in order to avoid a negative value. Accordingly, the eddy diffusivity used in the computations is actually given by

$$\nu_{\mathrm{T}} = \max\left(C_r^2 \Delta^2, 0\right) |\tilde{\mathsf{S}}|. \tag{28}$$

Also note that the integral approximation in (21) is also used to evaluate the SFS vorticity source term in Eq. (12); this yields

$$\begin{aligned} &D[\nu_{\mathrm{T}}, \zeta](\boldsymbol{X}_i) \\ &\quad = \max\left(C_r^2 \Delta^2 |\tilde{\mathsf{S}}|, 0\right) \frac{1}{\delta^2} \sum_{j=1}^{N} \sqrt{|\tilde{\mathsf{S}}(\boldsymbol{X}_i)||\tilde{\mathsf{S}}(\boldsymbol{X}_j)|}(\tilde{\boldsymbol{\omega}}(\boldsymbol{X}_j) - \tilde{\boldsymbol{\omega}}(\boldsymbol{X}_i))\, dV_j g_\delta(\boldsymbol{X}_j - \boldsymbol{X}_i). \end{aligned} \tag{29}$$

This completes the description of the particle approximation.

2.5. *Local Mesh Refinement*

The computations discussed below incorporate a local mesh refinement scheme which combines particle-splitting and particle-merging algorithms. The particle-splitting algorithm essentially amounts to locally distributing the vorticity into a larger number of particles whenever these particles are subjected to large strain. It aims at ensuring that neighboring particles have overlapping cores and consequently that an adequate particle representation is maintained despite severe deformation of the flow map. Prior computations (e.g., [13, 21, 22]) indicate that such local refinement schemes are effective in avoiding rapid deterioration of the accuracy of the calculations associated with loss of core overlap. In complex flows, however, mesh refinement may lead to excessive growth in the number of computational elements and in CPU time. The particle-merging algorithm is introduced in order to avoid such a phenomenon. It essentially consists of reducing the number of particles in regions where the particles tend to cluster.

The particle-splitting algorithm used in the present work is motivated by earlier experiences with filament-based algorithms [1, 2, 22], which generally base splitting criteria on the length of individual segments. As mentioned above, a particle-based representation which does not explicitly track the relative positions of the computational elements is used in the present work; thus, a new mesh refinement scheme is introduced. The scheme mimics the action of segment splitting by assigning to each particle three vectors $\delta\boldsymbol{\chi}^k(t)$, $k = 1, 2, 3$, whose evolution reflects the local deformation. These vectors are regarded as infinitesimal material segments originating at the center of each particle. Initially, the vectors are mutually orthogonal, have unit length, and are aligned with the basis vectors $\boldsymbol{e}^k$, $k = 1, 2, 3$, of a right-handed Cartesian coordinate system in which the motion is described. We thus have $\delta\boldsymbol{\chi}^k(0) = \boldsymbol{e}^k$, $k = 1, 2, 3$. As the particles are transported by the flow, the evolution of the corresponding elementary vectors is governed by

$$\frac{D}{Dt}\delta\boldsymbol{\chi}_i^k = \delta\boldsymbol{\chi}_i^k \cdot \nabla\boldsymbol{u}(\boldsymbol{X}_i), \; k = 1, 2, 3; \tag{30}$$

i.e., the “normalized” material segments stretch and tilt according to the local strain field.

Based on the evolution of $\delta\chi_i^k$, a Lagrangian strain tensor E is formed using

$$\mathsf{E} \equiv \frac{1}{2}\{\mathsf{U} + \mathsf{U}^{\mathrm{T}} + \mathsf{U}\mathsf{U}^{\mathrm{T}}\}, \tag{31}$$

where

$$\mathsf{U} \equiv \left[\frac{\delta\boldsymbol{\chi}^1(t) - \delta\boldsymbol{\chi}^1(0)}{|\delta\boldsymbol{\chi}^1(0)|}\middle|\frac{\delta\boldsymbol{\chi}^2(t) - \delta\boldsymbol{\chi}^2(0)}{|\delta\boldsymbol{\chi}^2(0)|}\middle|\frac{\delta\boldsymbol{\chi}^3(t) - \delta\boldsymbol{\chi}^3(0)}{|\delta\boldsymbol{\chi}^3(0)|}\right] \tag{32}$$

and the superscript T denotes the transpose. The eigenvectors of E are the principal strain axes.

The splitting of vortex particles is directly based on the eigenvalues of E. Specifically, splitting is performed when the largest eigenvalue exceeds $\frac{3}{2}$, i.e., when the particle has stretched to twice its original length along the corresponding eigenvector. This can be illustrated with the simple example of a particle being stretched along the x-axis by a velocity field with constant velocity gradient,

$$\nabla\boldsymbol{u} = \begin{bmatrix} 1 & 0 & 0 \\ 0 & -1 & 0 \\ 0 & 0 & 0 \end{bmatrix}. \tag{33}$$

Following Eq. (32), the material segments are given by

$$\delta\boldsymbol{\chi}^1(t) = [\,e^t \quad 0 \quad 0\,]^{\mathrm{T}} \tag{34}$$

$$\delta\boldsymbol{\chi}^2(t) = [\,0 \quad e^{-t} \quad 0\,]^{\mathrm{T}} \tag{35}$$

$$\delta\boldsymbol{\chi}^3(t) = [\,0 \quad 0 \quad 1\,]^{\mathrm{T}}. \tag{36}$$

At time $t = \log_e 2$, the vector $\delta\boldsymbol{\chi}^1$ has twice its original length, and the tensor U is

$$\mathsf{U} = \begin{bmatrix} 2-1 & 0 & 0 \\ 0 & \frac{1}{2}-1 & 0 \\ 0 & 0 & 1-1 \end{bmatrix} = \begin{bmatrix} 1 & 0 & 0 \\ 0 & -\frac{1}{2} & 0 \\ 0 & 0 & 0 \end{bmatrix}. \tag{37}$$

The strain tensor E is then

$$\mathsf{E} = \begin{bmatrix} \frac{3}{2} & 0 & 0 \\ 0 & -\frac{3}{8} & 0 \\ 0 & 0 & 0 \end{bmatrix}. \tag{38}$$

The eigenvalues of E at this time are $3/2$, 0, and $-3/8$. The eigenvector corresponding to the eigenvalue $3/2$ is $\boldsymbol{e}^1$, the direction in which the particle was stretched to twice its original length. In general, rotation and stretching lead to more involved expressions but the above observation still holds; i.e., if an eigenvalue of E reaches $3/2$, then the particle has "stretched" to twice its original length along the corresponding eigenvector.

Once the leading eigenvalue of E exceeds $3/2$ the particle is split into two daughter particles. They are placed a distance $h_0/2$ away from their parent, along the principal strain axis. h_0 is the Cartesian grid size used to discretize the vorticity field at the start of the calculations. Each daughter receives half the volume of their mother and the same vortex strength. The material segment vectors on each daughter particle are reset to the orthonormal configuration.

In complex flows, such as the ring collisions of the following section, particle splitting leads to rapid and excessive growth in the number of particles. To control this a particle-merging scheme is used. Introduction of the merging scheme is motivated by recent hairpin (or scale) removal experiences in filament-based computations [1–6, 8], though the present procedure appears as a simplified version of filament remeshing. In the computations below, two particles are merged into one whenever the separation distance falls below a threshold β. (In the computations, we set $\beta = h_0/2$.) If particles i and j satisfy this criterion, they are replaced with a single particle whose position, volume, and strength are given by

$$\begin{aligned} \boldsymbol{X}_{ij} &= \frac{\boldsymbol{X}_i|\zeta_i|\,dV_i + \boldsymbol{X}_j|\zeta_j|\,dV_j}{|\zeta_i|\,dV_i + |\zeta_j|\,dV_j} \\ dV_{ij} &= dV_i + dV_j \end{aligned} \tag{39}$$

$$\zeta_{ij} = \frac{\zeta_i\,dV_i + \zeta_j\,dV_j}{dV_i + dV_j}, \tag{40}$$

respectively. It is easy to verify that the volume of vorticity is unaffected by merging or splitting, but that neither the splitting or the merging procedure conserves enstrophy or kinetic energy.

Implementation of the merging scheme necessitates an extension of the splitting scheme, since elementary segments $\delta\boldsymbol{\chi}^k$, $k = 1, 2, 3$, for the merged particles must be defined. To this end, we combine the segments $\delta\boldsymbol{\chi}_i$ and $\delta\boldsymbol{\chi}_j$ of the two consolidating particles i and j. First, the three vectors corresponding to the smaller particle are scaled by the factor dV_j/dV_i, where $dV_i > dV_j$. Second, the largest of the six vectors is selected as the major semiaxis, $\boldsymbol{v}^{\mathsf{A}}$, of an ellipsoid, with the unit vector in this direction being $\boldsymbol{e}^{\mathsf{A}}$. Third, two mutually orthogonal unit vectors, $\boldsymbol{e}^{\mathsf{B}}$ and $\boldsymbol{e}^{\mathsf{C}}$, are constructed in the plane perpendicular to the major semiaxis. The semiminor semiaxes of the ellipsoid, $\boldsymbol{v}^{\mathsf{B}}$ and $\boldsymbol{v}^{\mathsf{C}}$, are taken to be in the directions of $\boldsymbol{e}^{\mathsf{B}}$ and $\boldsymbol{e}^{\mathsf{C}}$. Fourth, the length of $\boldsymbol{v}^{\mathsf{B}}$ is found as the shortest length such that

$$\left(\frac{\delta\boldsymbol{\chi}^k\cdot\boldsymbol{e}^{\mathsf{A}}}{|\boldsymbol{v}^{\mathsf{A}}|}\right)^2 + \left(\frac{\delta\boldsymbol{\chi}^k\cdot\boldsymbol{e}^{\mathsf{B}}}{|\boldsymbol{v}^{\mathsf{B}}|}\right)^2 + \left(\frac{\delta\boldsymbol{\chi}^k\cdot\boldsymbol{e}^{\mathsf{C}}}{|\boldsymbol{v}^{\mathsf{B}}|}\right)^2 \le 1,\ k = 1, \ldots, 6. \tag{41}$$

In other words, all six segments fit inside an ellipsoid whose major semiaxis has length $|\boldsymbol{v}^{\mathsf{A}}|$ and whose cross-section through its center, perpendicular to the major axis, is a circle with radius $|\boldsymbol{v}^{\mathsf{B}}|$. Last, the length of $\boldsymbol{v}^{\mathsf{C}}$ is calculated as the shortest length such that

$$\left(\frac{\delta\boldsymbol{\chi}^k\cdot\boldsymbol{e}^{\mathsf{A}}}{|\boldsymbol{v}^{\mathsf{A}}|}\right)^2 + \left(\frac{\delta\boldsymbol{\chi}^k\cdot\boldsymbol{e}^{\mathsf{B}}}{|\boldsymbol{v}^{\mathsf{B}}|}\right)^2 + \left(\frac{\delta\boldsymbol{\chi}^k\cdot\boldsymbol{e}^{\mathsf{C}}}{|\boldsymbol{v}^{\mathsf{C}}|}\right)^2 \le 1,\ k = 1, \ldots, 6. \tag{42}$$

The material segments of the consolidated particle, $\delta\boldsymbol{\chi}_{ij}^1$, $\delta\boldsymbol{\chi}_{ij}^2$, and $\delta\boldsymbol{\chi}_{ij}^3$, are taken to be the semiaxes of the ellipsoid, $\boldsymbol{v}^{\mathsf{A}}$, $\boldsymbol{v}^{\mathsf{B}}$, and $\boldsymbol{v}^{\mathsf{C}}$, respectively.

2.6. *Parallel Implementation*

Simulations using the present scheme were performed on the CRAY T3D at the Pittsburgh Supercomputer Center. The methodology used to construct and optimize parallel codes has been directly adapted from [23]. Its essential features consist in distributing the particle data among all available processors. The particle data are organized into arrays which are distributed among all the processors following a cyclic distribution scheme; machine-specific directives are used for this purpose. A duplicate copy of the *local* data is also created at the start of the parallel computations and placed in scratch arrays. Scratch arrays for partial convolution sums are also defined. During the parallel computations, each processor computes binary interactions using the particle data that is resident on its memory. Once the local interactions are computed, each processor communicates to its neighbor the data in the scratch arrays. The computation of local interactions and the communication step define an elementary iteration, which is repeated until the particle data has visited all the processors. At this stage, the necessary convolutions are computed based on the (local) partial sum results, and numerical integration of the discrete equation is performed locally using the resident data.

In addition to providing a detailed description of the parallel algorithm above, Ref. [23] also discusses an extensive performance study. In particular, it is shown that the above approach results in efficient algorithms with excellent scalability properties. Typically, the computations below are performed on a 64-processor partition, with a total number of elements ranging from 4×10^3 to 10^5. High (>0.9) parallel efficiency is maintained as long as the number of particles per processor is larger than about 100. At these conditions, the performance of the calculations is around 30 MFlops per processor.

3. RESULTS

The numerical scheme described in the previous section is applied to LES of isolated and colliding vortex rings. In the case of the isolated vortex ring, the scheme is used to compute the self-induced propagation of the ring as well as the growth of 3D azimuthal perturbations [22, 24]. Meanwhile, simulations of ring collisions are extended into late stages, where severe deformation of the vorticity field, including local cancellation and reconnection, is expected to occur [12]. We start with an illustration of the essential flow features (3.1) and then examine the behavior of the dynamic SFS model (3.2). We conclude (Section 3.3) with a discussion of the evolution of the enstrophy and kinetic energy, together with a brief examination of energy spectra.

3.1. *Basic Flow Features*

The evolution of the flow is illustrated by plotting at selected time instants the positions of the Lagrangian particles and/or surfaces of constant enstrophy. The constant-enstrophy surfaces are shown in 3D perspective views while the particle positions are presented as 2D scatter plots of *projected* particle positions. We generate projections on a streamwise plane (x–y) and on an azimuthal plane (z–y). The convention used is that the projection planes are identified by the corresponding normal vectors and that the axis of the vortex ring(s) coincides with the z-axis. When generating projections on the streamwise x–y plane, we mark the projected locations of *all* the Lagrangian particles. On the other hand, projections

TABLE I

Ring Parameters

σ/R	Core to radius ratio	0.275
Re_Γ	Γ/ν	2,200
Re_D	VD/ν	1,000
ϵ/R	Normalized perturbation amplitude	0.02
N_w	Wavenumber of perturbation	12
h_0/R	Normalized grid size	0.01

Note. R is the ring radius, σ is the core radius, Γ is the circulation, V is the self-induced propagation velocity, ν is the kinematic viscosity, ϵ is the perturbation amplitude, N_w is the number of azimuthal bending waves, and h_0 is the size of the Cartesian grid used for the initial discretization.

on the z–y plane only depict the projected location of *neighboring* particles, namely those lying within a distance δ from the plane of the projection. As can be appreciated from the results below, the streamwise projections generated in this fashion gives an illustration of secondary motion, while z–y projections effectively depict an azimuthal slice of the vortex core.

Isolated Vortex Ring. The physical parameters characterizing the vortex ring are summarized in Table I. We start with an axisymmetric vortex ring with core to radius ratio $\sigma/R = 0.275$. The Reynolds number based on the ring circulation is $\mathrm{Re}_\Gamma = 2{,}200$, while the Reynolds number based on ring diameter and self-induced translation velocity is $\mathrm{Re}_D = 1{,}000$. The initial distribution of azimuthal vorticity in the core of the ring is shown in Fig. 1. Prior to the calculations, the ring vorticity is perturbed in the azimuthal direction by displacing the axis of the vortex core using a sinewave perturbation [22]. The bending wave perturbation is specified in terms of its amplitude, ϵ, and wavenumber, N_w. As shown in Table I, a perturbation with $\epsilon/R = 0.02$ and $N_\mathrm{w} = 12$ is selected. For the present ring parameters [22], this value of N_w corresponds to the most amplified mode of the Widnall instability [24]. The vorticity distribution of the perturbed vortex ring is discretized onto Lagrangian particles that are initially distributed on a uniform Cartesian mesh of cell size, h_0. Vortex particles whose strength falls below 1% of the peak particle strength are omitted. For the present ring, there are 4155 particles at the start of the calculation.

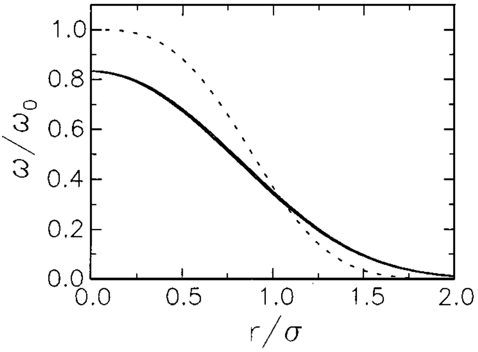

FIG. 1. Solid line: initial azimuthal vorticity profile in the core of the ring. The dotted line shows the core smoothing function. r is the radial distance in the azimuthal plane, measured from the center of the core.

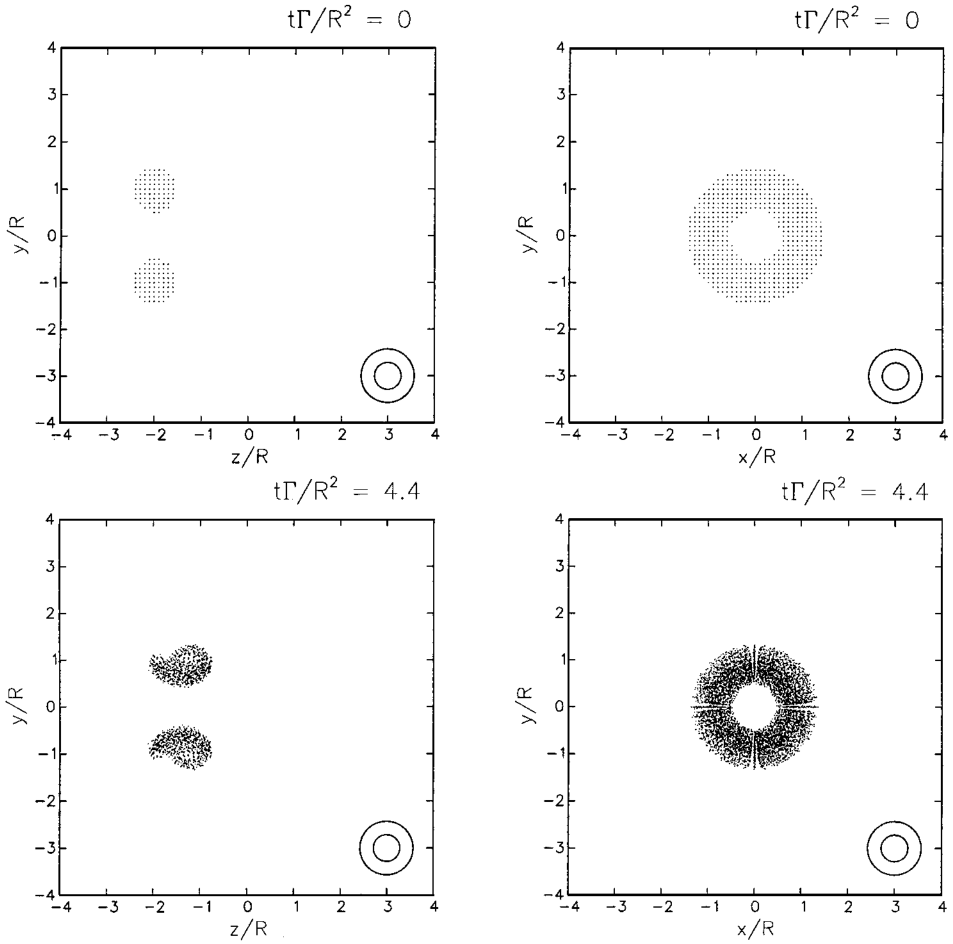

FIG. 2. Particle locations for single translating ring with turbulence model. Plotted on the left are projections on the z–y plane of Lagrangian particles lying in the slice $-\Delta \le x \le \Delta$. The right column shows the projection of all the particles on the x–y plane. The concentric circles in the lower-right corner show the size of the particle filter, Δ, and the test filter, 2Δ.

The evolution of the perturbed vortex ring is illustrated in Fig. 2, which shows the distribution of vortex particles at selected times, and in Fig. 3 which depicts three-dimensional perspective views of surfaces of constant vorticity. The vorticity surfaces are plotted using the same scale and the same vorticity level and the particle plots are generated using the same scale. The initial four-sector symmetry seen in the particle plots is due to the initial placement on a Cartesian grid. This symmetry is not noticeable in the vorticity field.

Figure 2 shows that during the course of the simulation the vortex ring travels, from right to left, a distance of about two ring diameters. As the ring propagates, the volume occupied by vortex particles expands to include the space between the core and the ring axis. Meanwhile, the ring diameter does not appear to change. Figure 2 also shows that some particles are left in the wake of the ring. These particles contain little vorticity and the wake appears to have little effect on the dynamics of the vortex cores. This was shown by repeating some of the simulations with particles in the wake removed. The removal made essentially no difference in the evolution of the particles within the vortex cores.

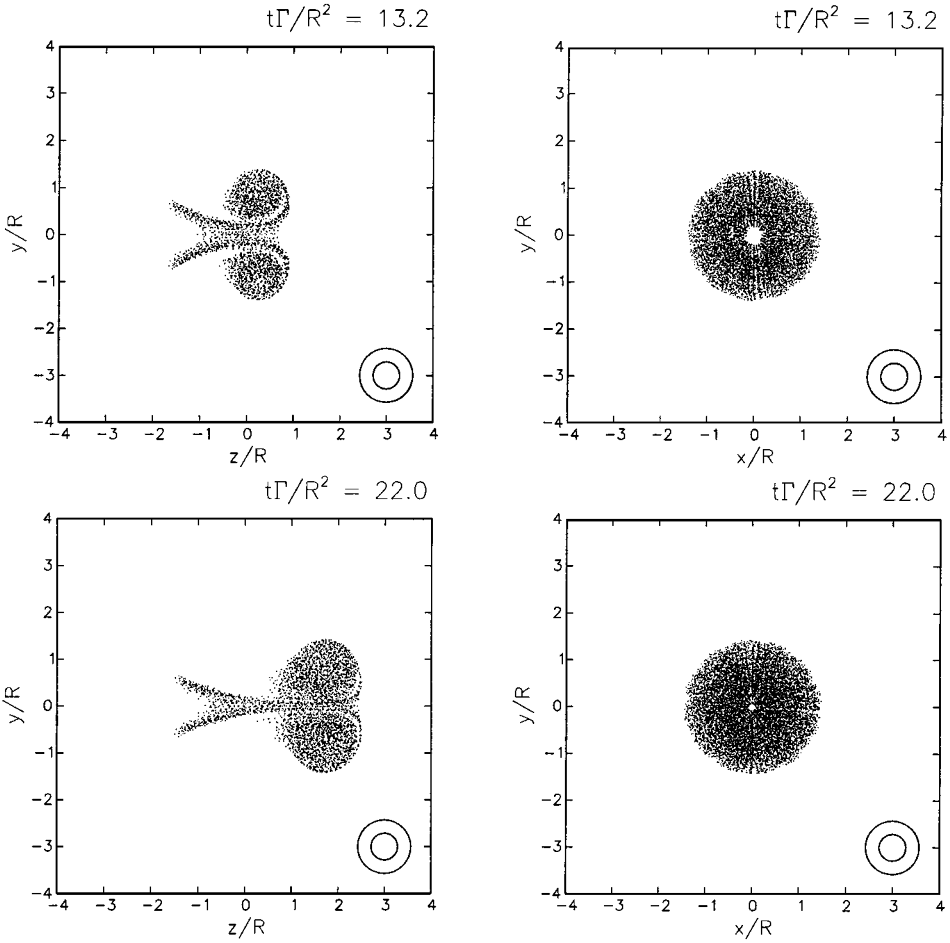

FIG. 2—*Continued*

Figure 3 shows that little change in the shape of the isolated vortex ring occurs during the simulation. In particular, the thickness of the ring, as perceived from the surface plots, appears to remain unchanged. The growth of the perturbation is clearly evident but, as mentioned earlier, the deformation of the ring remains small. This suggests that within the duration of the computation the vortex ring remains laminar; this is further examined below in Section 3.2 in light of dynamic computations of turbulent eddy viscosity.

Colliding Vortex Rings. The initial setup in colliding ring simulations consists of two coaxial vortex rings initially placed “upstream” and “downstream” of the plane $z = 0$. The centroids of the vortex rings are initially at a distance of one ring diameter from the plane of collision. We focus on collisions of initially perturbed vortex rings. Without perturbation, transition to turbulence was not observed as the colliding rings approach each other, slow down and stretch while maintaining perfect axial symmetry. These simulations are thus omitted.

The vortex ring lying in the half-space $z < 0$ is an identical copy of the perturbed vortex ring described above. The second vortex ring is an “image” of the first which is specified in terms of a mapping. Two mappings are considered in the present study. In the

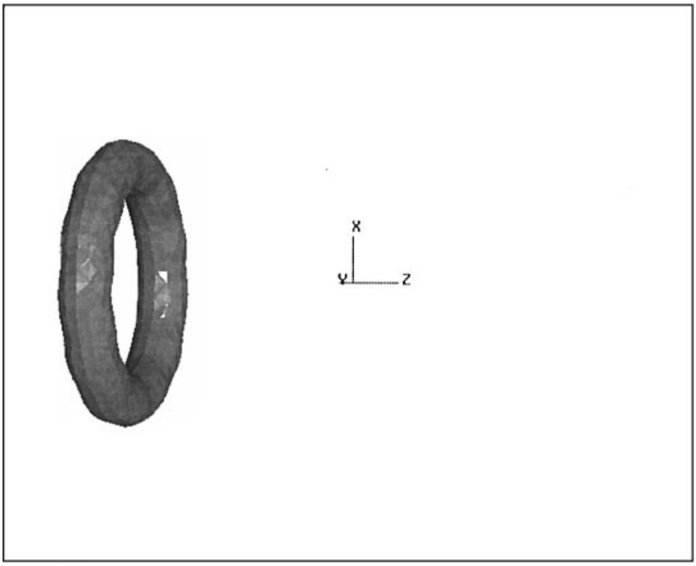

$t\Gamma/R^2 = 0$

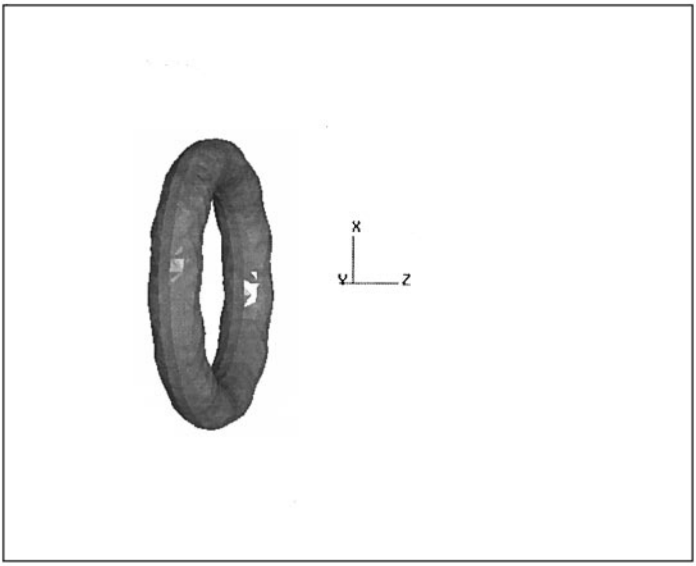

$t\Gamma/R^2 = 4.4$

FIG. 3. Surface of constant vorticity magnitude ($\|\boldsymbol{\omega}\| R^2/\Gamma = 1.82$) for an isolated vortex ring with turbulence model.

first mapping, the second ring is generated by reflecting the particles of the first ring with respect to the plane $z = 0$. Thus, the particles positions are mapped in Cartesian coordinates according to $(x, y, z) \to (x, y, -z)$. Meanwhile, the particle strengths are mapped by $(\zeta_x, \zeta_y, \zeta_z) \to (-\zeta_x, -\zeta_y, \zeta_z)$. Note that for this mapping the azimuthal sinewave perturbation on both rings are in phase. Thus, as the rings approach each other the crest of

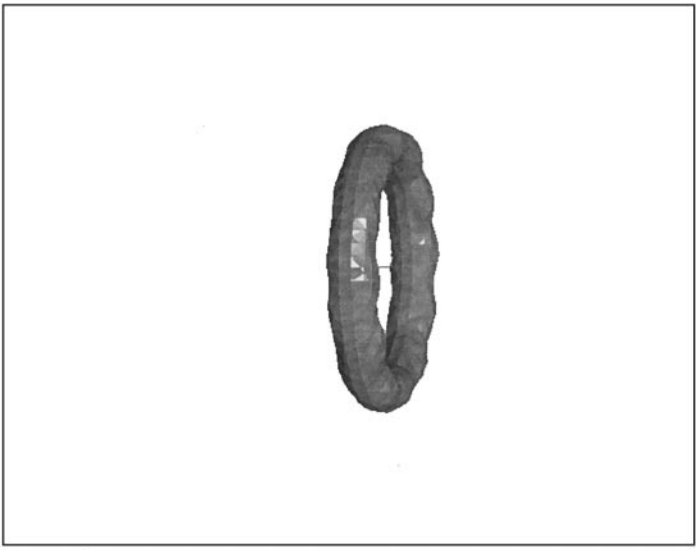

$t\Gamma/R^2 = 13.2$

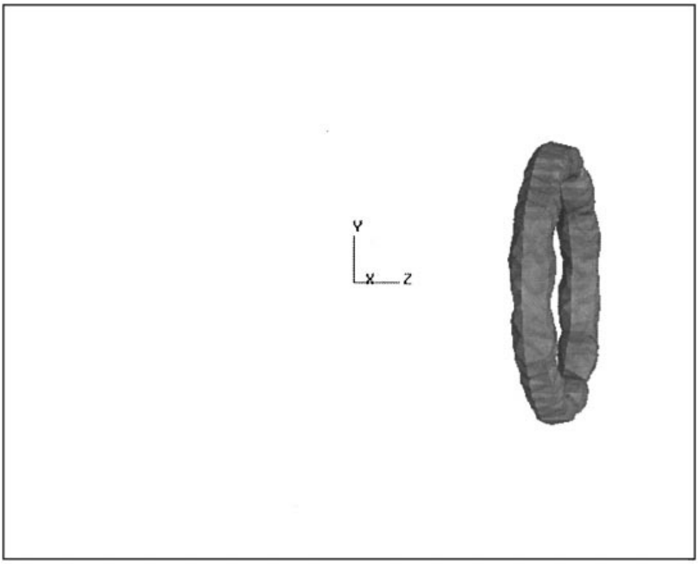

$t\Gamma/R^2 = 22$

FIG. 3—*Continued*

these waves tend to collide first, and the arrangement is therefore referred to as crest-to-crest alignment or collision. On the other hand, a second mapping is implemented so that the sinewaves are aligned crest-to-trough, i.e., the perturbations of the rings are out of phase. In this case, the particle positions and strengths are rotated in the azimuthal direction by an angle π/N_{w}. This mapping twists one of the rings half a perturbation wavelength. While other twisting angles were considered in the calculations, we restrict our attention to the cases with crest-to-crest and crest-to-trough alignments and perform the simulations both with and without SFS model. Thus, four cases are contrasted in the discussion below.

We start with results obtained for a crest-to-crest collision without turbulence model and plot in Fig. 4 the particle locations at selected time instants. In the early stages of the simulation, the rings propagate under their own self-induced motion, and particles with low vorticity are left in the wakes of the rings. As the rings approach each other, their translation velocity decreases while their radii increase. As discussed later, this also leads to significant increase in the enstrophy. By $t\,\Gamma/R^2 = 17.6$, the two rings can no longer be distinguished as they have completely merged into a single doughnut-shaped structure. This structure continues to extend in the radial direction, leaving a web of particles around the centers. Like the particles left in the wakes of the approaching rings, these particles carry little vorticity and have consequently little effect on the dynamics of the concentrated cores. This was tested by repeating some simulations with the particles in the wake of the rings removed. Figure 4 shows that at $t\,\Gamma/R^2 = 19.8$ the particles have clumped into 12 groups spaced azimuthally in correspondence with the initial perturbation of the rings. The clumping is also evident in the last frame ($t\,\Gamma/R^2 = 22$), which also shows that irregularities appear in the positions of the particles.

In the early stages of the simulation the rings are well separated and the interaction is weak. Thus, results for the various cases are quite similar, and differences are only observed at later stages. Thus, in discussing the results of the other three cases we omit the early stages of approach towards the plane of collision and focus exclusively on the later stages.

Figure 5 shows distributions of the Lagrangian particles at selected times for the simulation of crest-to-crest vortex ring collision with turbulence model. The results show that the distribution of particles during the simulation is qualitatively similar to that observed in the simulation without turbulence model. In particular, the stretching of the vortex rings, their merger and the generation of 12 distinct particle clusters are observed. However, the results also indicate that when the turbulence model is included this process occurs at a slower rate. This can be most easily appreciated by comparing in Figs. 4 and 5 the stretching of the ring radii at corresponding time instants.

Crest-to-trough vortex ring collisions are illustrated in Fig. 6, which shows particle distributions obtained from a simulation without turbulence model, and in Fig. 7, which shows similar distributions for a simulation with turbulence model. The results reveal several differences from the crest-to-crest collisions. In particular, the particle distributions in the crest-to-trough collision have a larger extent in the z-direction than in the crest-to-crest collision. Another distinctive feature of the crest-to-trough alignment is that in the late stages of the collision the particles distributions exhibit 24 distinct clumps; in the crest-to-crest collisions 12 clumps are instead obtained (Figs. 4 and 5). Thus, the initial alignment of the perturbation appears to have a significant effect on the evolution of the flow.

Meanwhile, comparison of Figs. 6 and 7 indicates that the particle distributions in crest-to-trough collisions simulated with and without turbulence model are similar, at least qualitatively. Close examination of the results suggests that, as observed for the crest-to-crest collisions above, stretching and merger of the rings during collision occur at a slower rate when the turbulence model is active. One can also observe that when the turbulence model is deactivated the clumps of particles are no longer distinct in the final stages of the collision (Fig. 6); in fact, the particle distribution at the end of the simulation shows organization at different scales, in a manner suggestive of turbulence. Meanwhile, when the turbulence model is included (Fig. 7) the particle distribution appears to be more organized than that obtained with the model omitted.

Additional insight into the evolution of the flow is gained by generating three-dimensional perspective views of a constant enstrophy surface. Results are shown in Fig. 8 for crest-to-crest collision without turbulence model, in Fig. 9 for crest-to-crest collision with turbulence model, in Fig. 10 for crest-to-trough collision without turbulence model, and in Fig. 11 for crest-to-trough collision with turbulence model. Instantaneous views are generated at the same times at which the corresponding particle distributions are plotted in Figs. 4–7 respectively.

Figures 8–11 provide another illustration of the various stages of the head-on collision of the vortex rings. In particular, the initial "quasi-steady" stages of the motion, the deceleration and the increase in ring diameter, and the subsequent merger of the rings are clearly depicted. In addition, the surface plots also enable us to further characterize the late stages of the collision. In particular, the results show that the clumping of particles observed earlier is in fact associated with vortex reconnection, which leads to the formation of small-scale structures. These phenomena occur differently in the various cases and enable us to distinguish between them. Specifically, in the crest-to-crest collision without turbulence model (Fig. 8), early signs of reconnection can be observed at $t\,\Gamma/R^2 = 19.8$. By the end of the simulation, $t\,\Gamma/R^2 = 22$, the perspective view shows the presence of distinct vortical structures, which correspond to the 12 clumps of particles seen in Fig. 4. When the turbulence model is included, Fig. 9 shows that reconnection occurs at later time. At $t\,\Gamma/R^2 = 22$, the colliding rings can still be distinguished, although early signs of reconnection can be detected. By $t\,\Gamma/R^2 = 24.2$, however, distinct reconnected vortical structures have formed, and the original rings no longer exist.

As shown in Figs. 10 and 11 the details of the reconnection are significantly different when the initial perturbations of the rings are out of phase. In this case, the perturbations amplify in a sinuous fashion during the collision, in a manner similar to the way the bends in a river grow. Each half-bend of the rings corresponds to one of the 24 clumps of particles seen in the corresponding particle distribution shown in Fig. 10. At $t\,\Gamma/R^2 = 22$ the original rings have totally disappeared, leaving a disorderly collection of smaller-scale vortical structures. On the other hand, when the turbulence model is included the growth of the perturbations, though still significant, occurs at a slower rate. Significant decay appears to take place before the final stages, where only weak and disorganized structures remain.

We finally note that in all cases considered the head-on collision of the rings naturally leads to the generation of small-scale flow structures and consequently strains the resolution of the computations. The generation of small-scale structure is affected by a variety of phenomena, including the radial stretching of the large-eddy cores, the amplification of 3D instabilities and vortex merger and reconnection. The effect of small-scale structures on the behavior of the solution, and the role of the turbulence model are further discussed below.

3.2. *Dynamic Model Coefficient and Eddy Viscosity*

Figure 12 shows instantaneous values of the dynamic model coefficient, C_r^2. Plotted are curves for the isolated vortex rings, and for colliding vortex rings with crest-to-crest and crest-to-trough alignments. As mentioned above, each of the colliding ring calculations was performed both with and without turbulence model. When the turbulence model is deactivated, however, estimates of the dynamic model coefficient and the eddy viscosity are

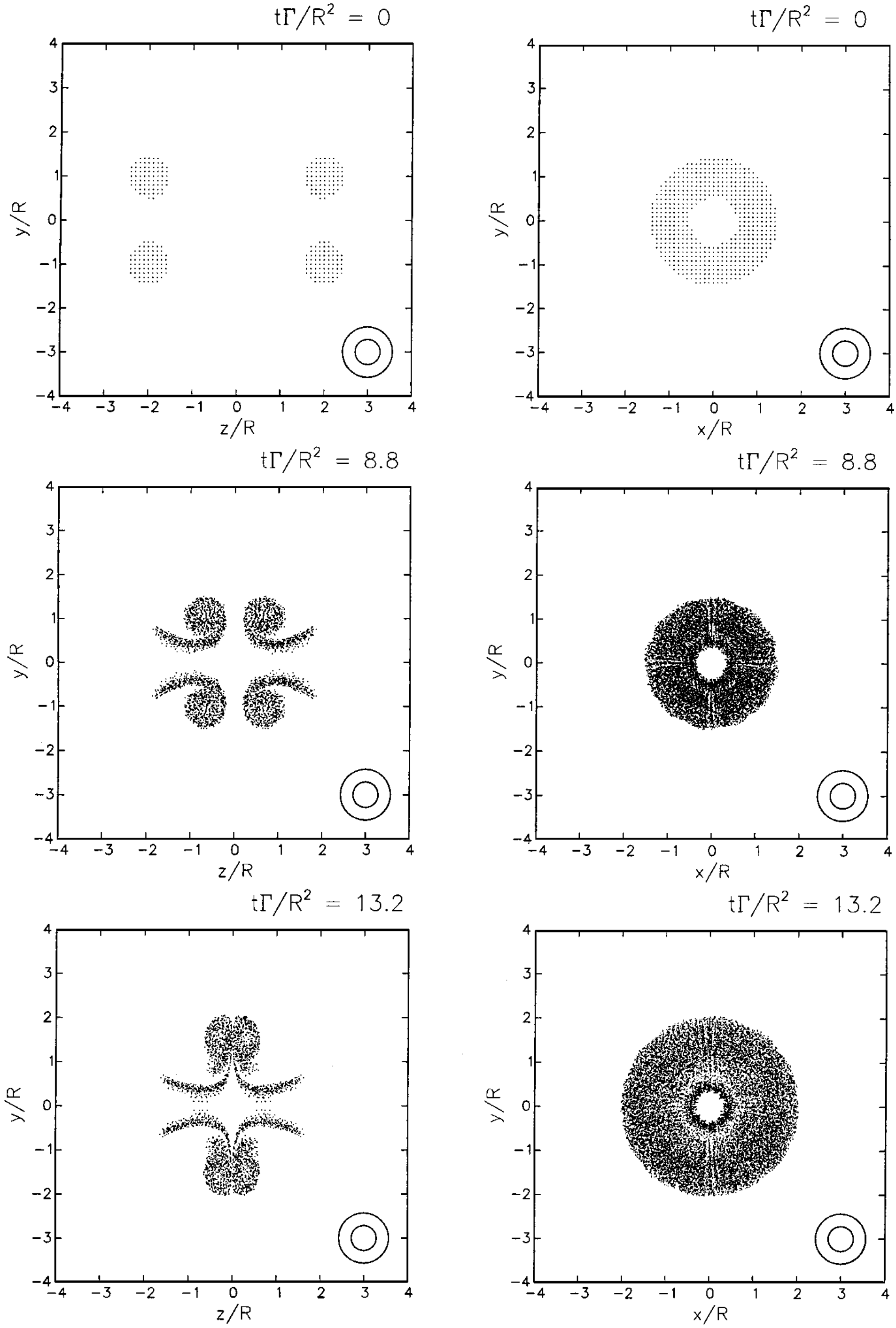

FIG. 4. Particle locations for crest-to-crest collision without turbulence model. Plotted on the left are projections on the z–y plane of Lagrangian particles lying in the slice $-\Delta \leq x \leq \Delta$. The right column shows the projection of all the particles on the x–y plane. The concentric circles in the lower-right corner show the size of the particle filter, Δ, and the test filter, 2Δ.

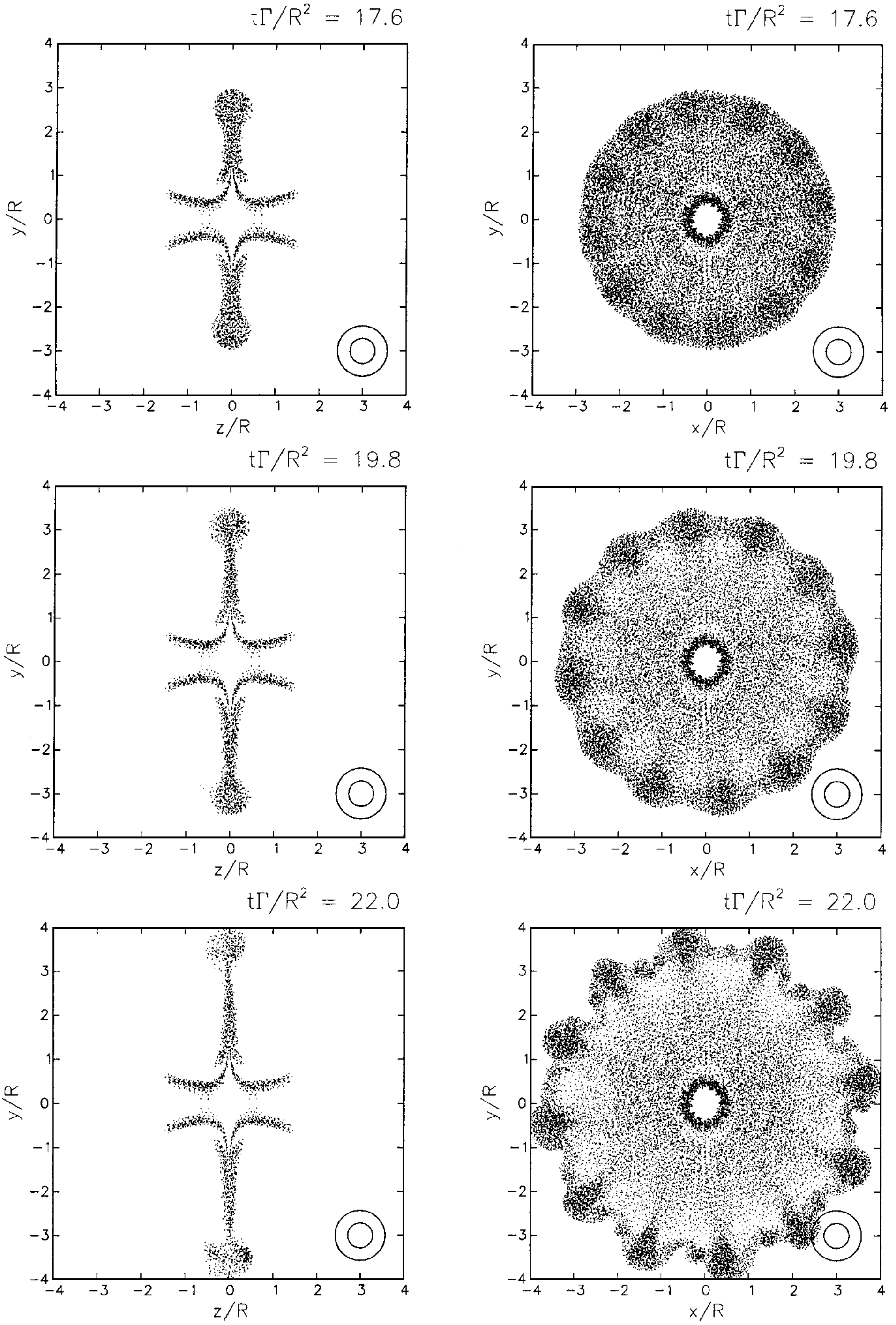
$t\Gamma/R^2 = 17.6$

$t\Gamma/R^2 = 17.6$

$t\Gamma/R^2 = 19.8$

$t\Gamma/R^2 = 19.8$

$t\Gamma/R^2 = 22.0$

$t\Gamma/R^2 = 22.0$

FIG. 4—*Continued*

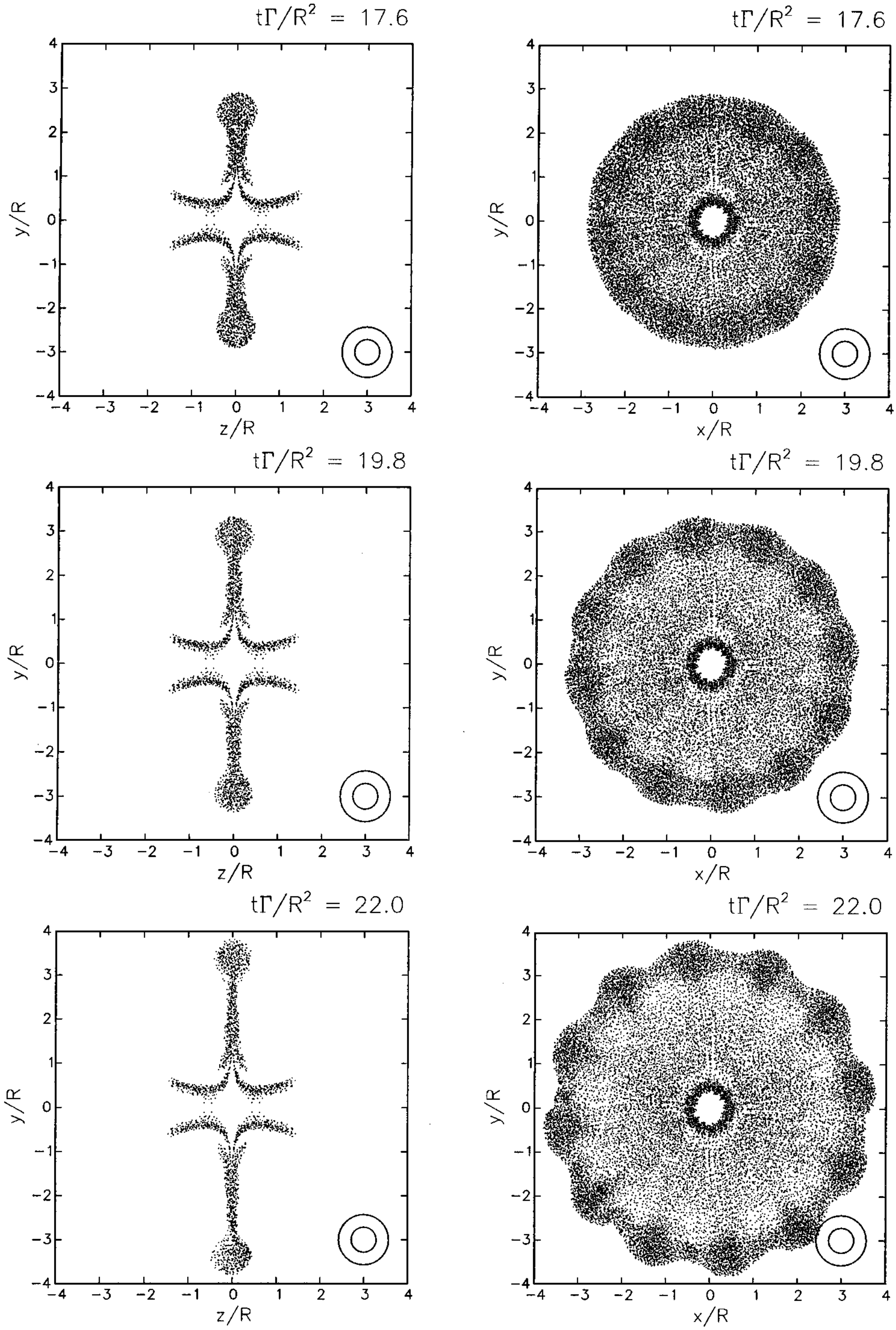

FIG. 5. Particle locations for crest-to-crest collision with turbulence model. The plots are generated as in Fig. 4.

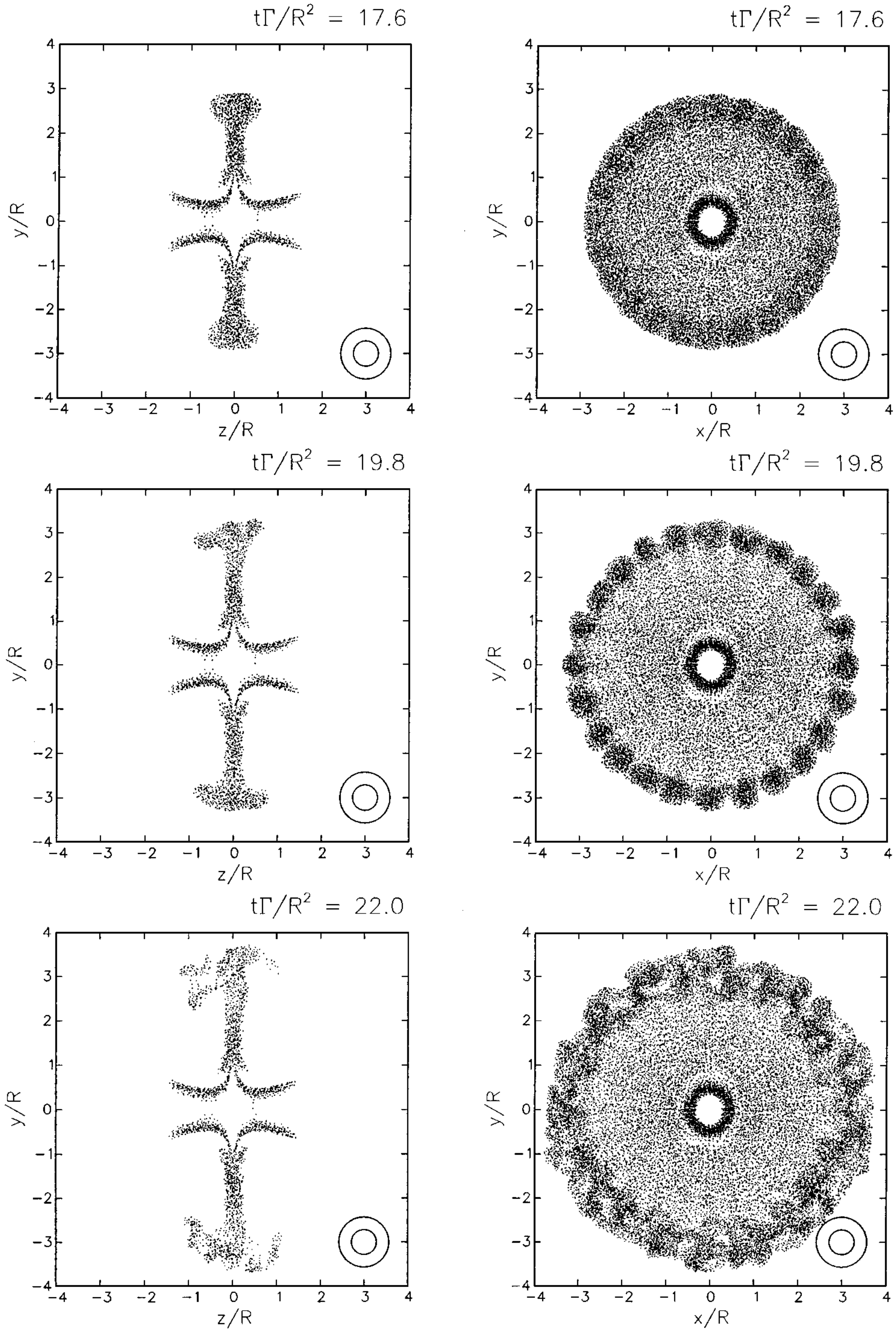

FIG. 6. Particle locations for crest-to-trough collision without turbulence model. The plots are generated as in Fig. 4.

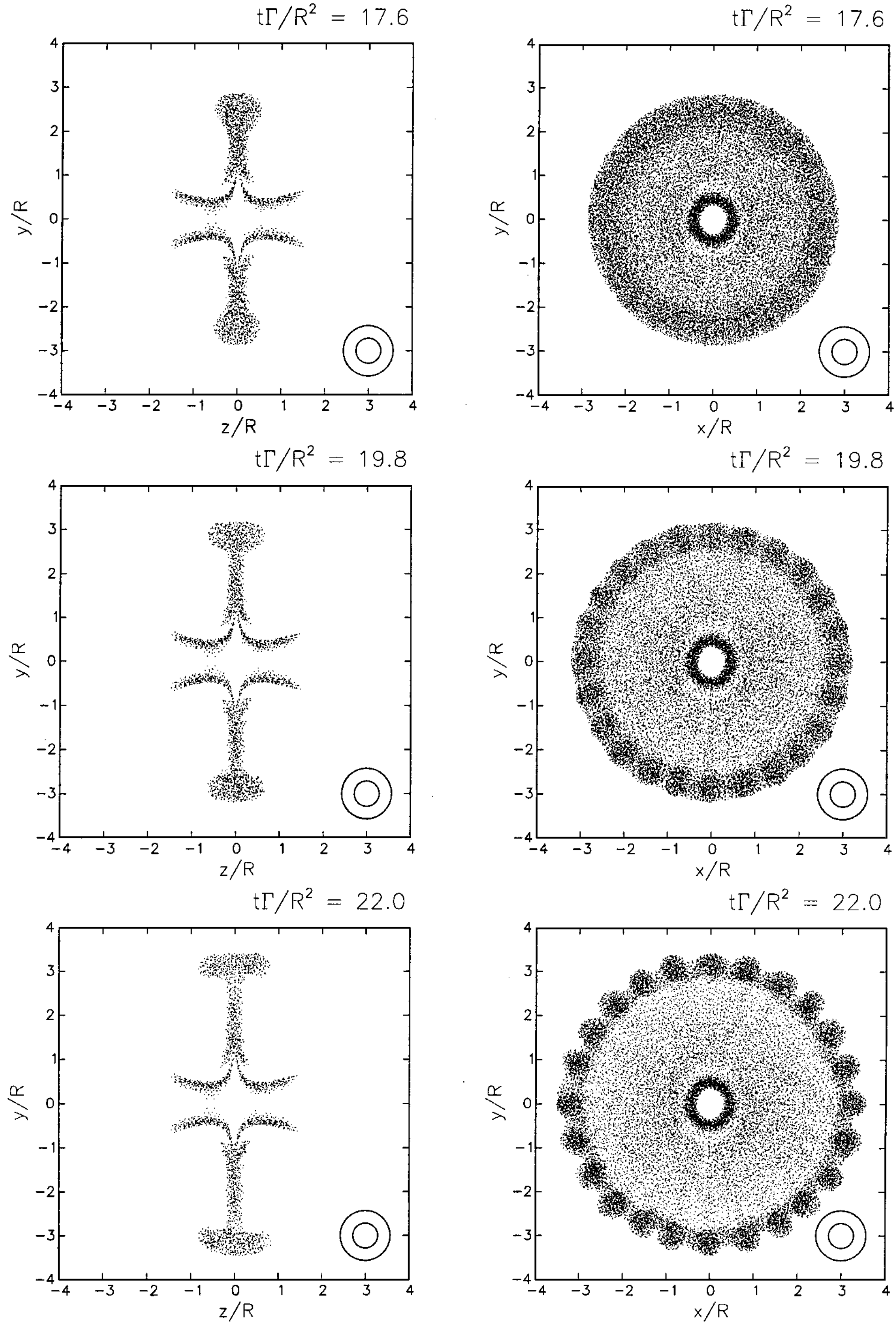

FIG. 7. Particle locations for crest-to-trough collision with turbulence model. The plots are generated as in Fig. 4.

nonetheless obtained, but are not used while updating the particle strengths. These estimates are also reported in Fig. 12.

In all cases considered, Fig. 12 shows that C_r is close to 0 at the start of the calculation. In the early stages, the computed estimate of C_r^2 first becomes negative, reaching a minimum around $t\,\Gamma/R^2 = 4.5$. (Recall that when the estimate of C_r^2 is negative ν_T is set to 0, as indicated in Eq. (28).) At later times, the curves for C_r^2 increase and positive values are reached around $t\,\Gamma/R^2 = 7$. Soon thereafter, the behavior of the curve for the isolated ring becomes different from those of the colliding ring calculations. For the single ring, C_r remains close to zero, whereas for the colliding rings, the coefficient increases in value. For the crest-to-crest alignment C_r^2 levels off, at $t\,\Gamma/R^2 = 13$, around 0.004, less than a third of the theoretical value for homogeneous, isotropic turbulence. The plateau lasts until $t\,\Gamma/R^2 = 16.5$ and then drops to zero. Simulations of the crest-to-trough collision also show a plateau in the value of C_r^2, but it lasts a shorter time, and after the plateau the coefficient continues to rise. It reaches a peak around $t\,\Gamma/R^2 = 17$ of about 0.008, half the theoretical value for homogeneous, isotropic turbulence. The model coefficient then gradually decreases for the rest of the simulation. Note that the theoretical value shown as a reference in Fig. 12 is valid for an ideal case, with Gaussian filter and inertial range scales. Deviations from this value may be expected to arise due to numerical discretization (which differs from filtering) and due to the fact that the resolution is not in an ideal inertial range.

For the purpose of quantifying the effect of C_r^2 on the simulation, we also examine the spatially averaged turbulence eddy viscosity, $\langle \nu_\mathrm{T} \rangle = C_r^2 \Delta^2 \langle |\tilde{\mathsf{S}}| \rangle$. (The strain-rate is a function of position in the flow field, but averages may be used for simple comparisons.) The average strain-rate modulus is plotted in Fig. 13 and $\langle \nu_\mathrm{T} \rangle / \nu$ is plotted in Fig. 14. The recorded values are particle averages, calculated directly based on the particle representation according to: $\langle |\tilde{\mathsf{S}}| \rangle = \sum_i |\tilde{\mathsf{S}}(X_i)|\, dV_i / \sum_i dV_i$. For the single ring, $\langle |\tilde{\mathsf{S}}| \rangle$ steadily decreases, dropping to 70% of its initial value at the end of the run. In the colliding ring simulations, $\langle |\tilde{\mathsf{S}}| \rangle$ first rises then decreases. Its maximum value is about 25% higher for simulations without the turbulence model than for those using the turbulence model. At later stages, the decrease is slower for crest-to-crest collisions than for the crest-to-trough cases.

The plots of turbulent eddy viscosity in Fig. 14 show the aggregate effects of the model coefficient and the strain-rate modulus. The variation of the eddy viscosity are dominated by changes in the model coefficient, whose relative variation has much greater range than that of the strain-rate modulus. The strain-rate modulus controls the spatial locations where the influence of the turbulence model is being experienced, as seen in the breakdown of the volume into quintiles according to vorticity magnitude. In low vorticity regions the turbulent eddy viscosity can be one or two orders of magnitude smaller than in high vorticity regions.

The indication from the dynamic model coefficient and the turbulent eddy viscosity is that the single, isolated ring is not turbulent. The rings colliding crest-to-crest may experience a degree of turbulence during their collision, which then dies off. The rings colliding crest-to-trough seem to experience a greater degree of turbulence in their collision, and it appears to last for longer time.

3.3. *Kinetic Energy and Enstrophy Evolution*

The evolution of the kinetic energy and enstrophy for the various cases is plotted in Fig. 15. These quantities are evaluated directly from the particle positions and strengths, as outlined in Appendix A. In the present calculations the flow is incompressible and unbounded, and

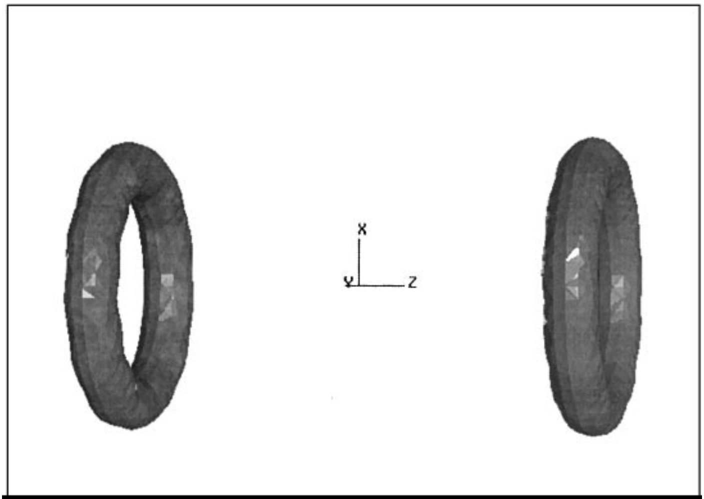

[redacted]

FIG. 8. Surface of constant vorticity magnitude ($\|\omega\| R^2/\Gamma = 1.82$) for crest-to-crest collision without turbulence model.

so there are no (physical) kinetic energy sources. Kinetic energy can be dissipated by both molecular viscosity and the turbulence model. Enstrophy is dissipated by molecular and eddy viscosity, but can also be generated by stretching of vortex lines. In addition, the particle representation is not conservative, and both the numerical discretization and the refinement/removal algorithm, may contribute to the evolution of the enstrophy and kinetic energy.

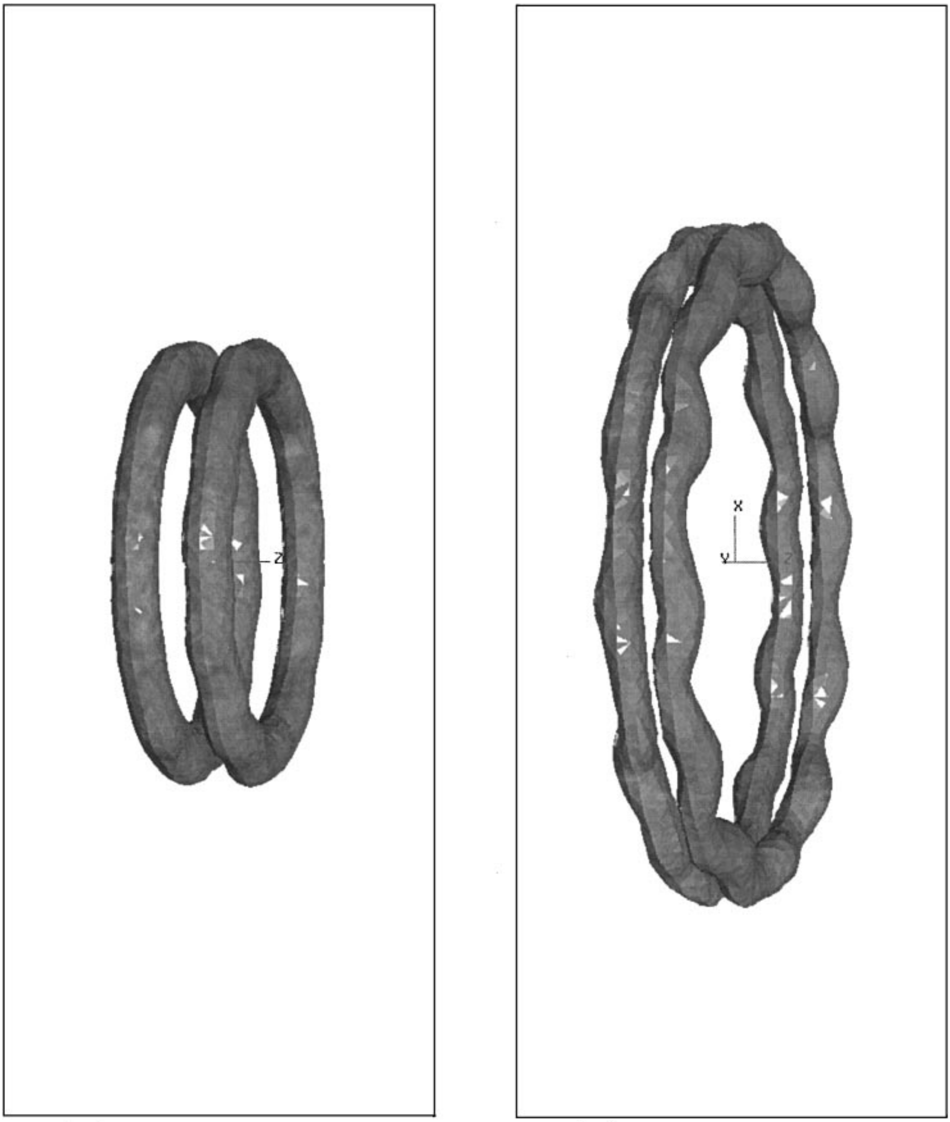

$t\Gamma/R^2 = 13.2$ $t\Gamma/R^2 = 17.6$

FIG. 8—*Continued*

Figure 15 shows that for the isolated vortex ring the kinetic energy experiences a steady monotonic decrease, amounting to a 14% drop by the end of the calculation. For the colliding ring simulations, the kinetic energy decreases in the initial stages at the same rate as for the single ring, but then the rate of decline increases. The kinetic energy for all four collision simulations is similar up to time $t\,\Gamma/R^2 = 15$ when the crest-to-crest collision simulation without a turbulence model begins to level off. The two collision simulations using the turbulence model also begin to level off at lower levels of kinetic energy. The crest-to-trough collision results in a lower level of kinetic energy than the crest-to-crest collision. The kinetic energy for the simulation without turbulence model of the crest-to-trough collision does not level off but after arriving at a minimum begins to rise quickly. This indicates severe

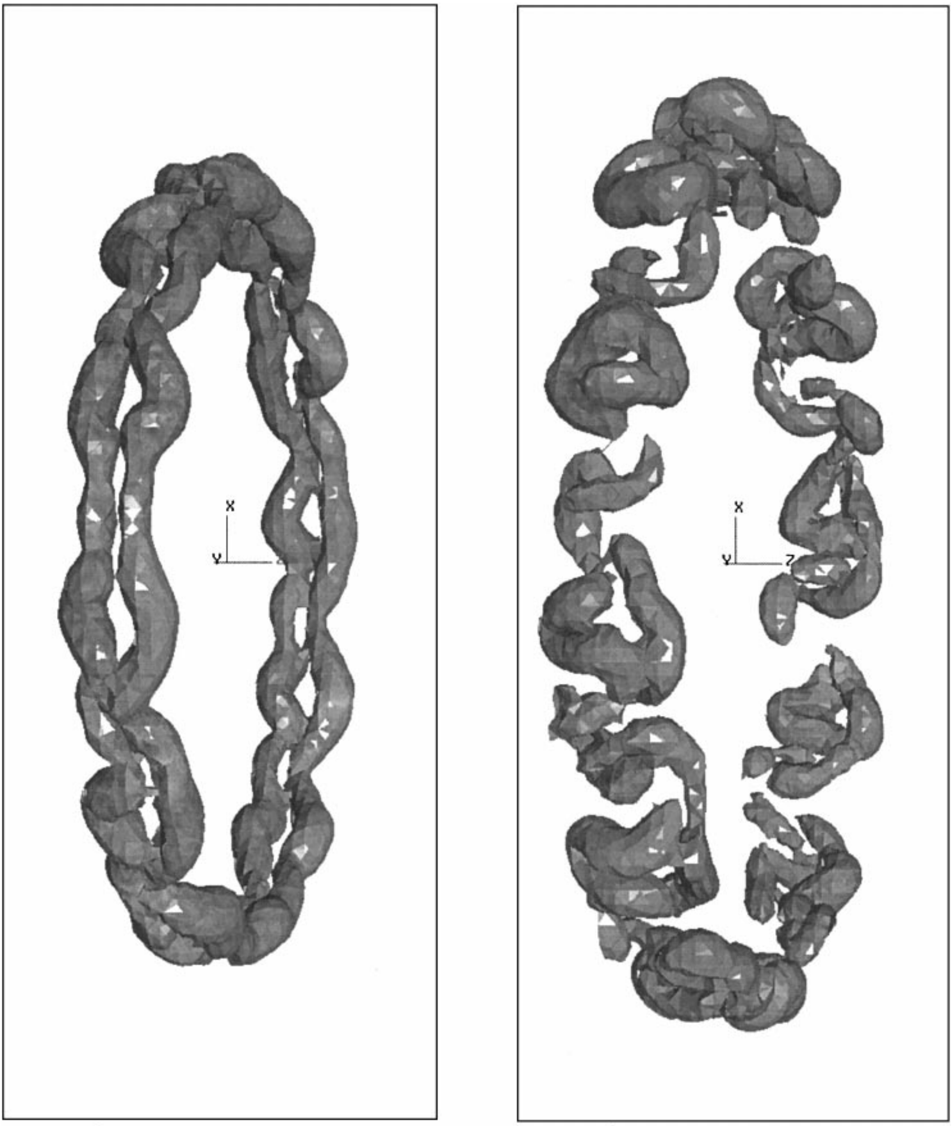

$t\,\Gamma/R^2 = 19.8$ $t\,\Gamma/R^2 = 22$

FIG. 8—*Continued*

deterioration in the particle representation since, as mentioned earlier, there are no sources of kinetic energy in the flow. At very large times, $t\,\Gamma/R^2 > 22$, the runs using the turbulence model also show a small, unphysical, rise in kinetic energy.

Figure 15 also shows that for the isolated ring the decay of kinetic energy is accompanied by a similar decay in the enstrophy, with a 29% drop at the end of the calculation. On the other hand, the enstrophy increases in the colliding ring calculations, indicating significant vortex stretching. When the turbulence model is applied, the enstrophy curve levels off by $t\,\Gamma/R^2 = 16$ and remains at about 160% its original level for the remainder of the calculation. For the crest-to-crest collision without turbulence model, a plateau in the enstrophy curve also occurs at $t\,\Gamma/R^2 = 16$, but at higher value; near the end of the

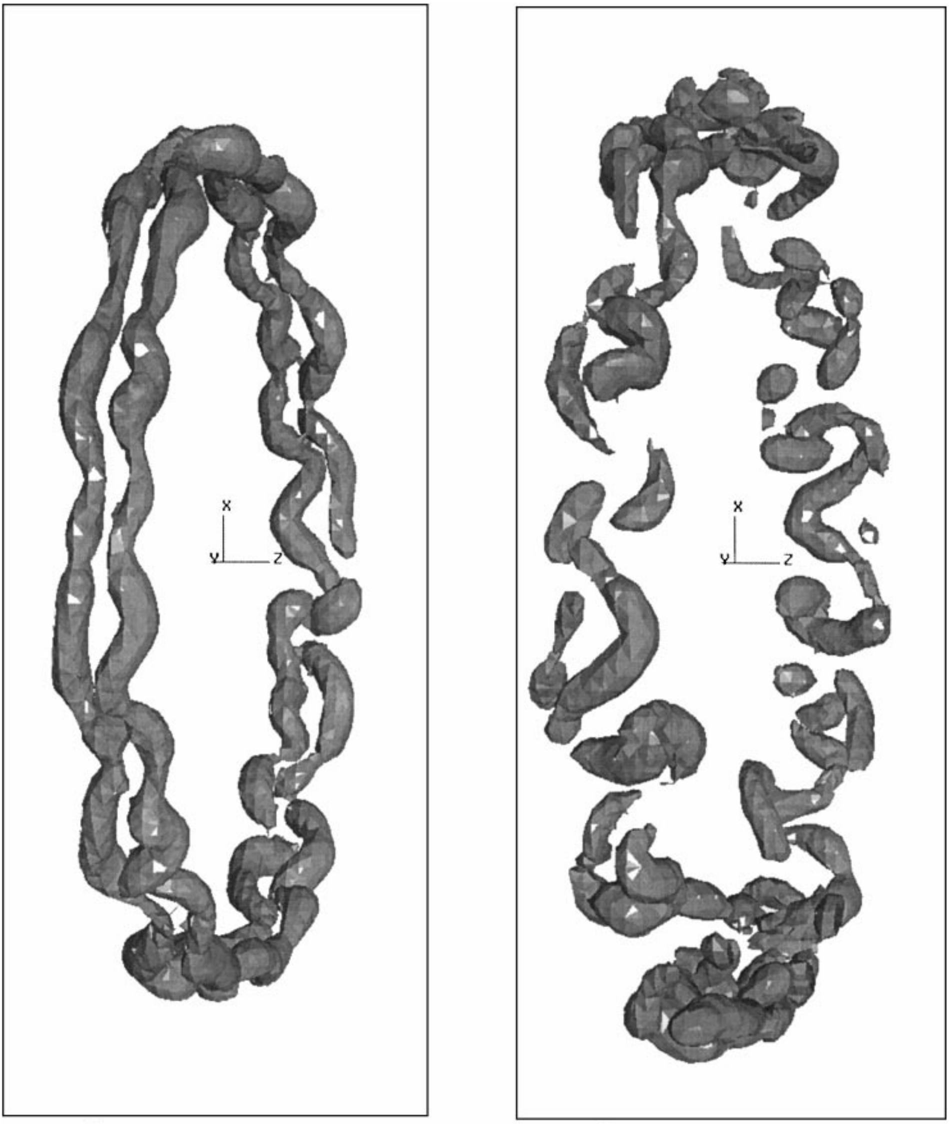

$t\Gamma/R^2 = 22$ $t\Gamma/R^2 = 24.2$

FIG. 9. Surface of constant vorticity magnitude ($\|\omega\| R^2/\Gamma = 1.82$) for crest-to-crest collision with turbulence model.

simulation, however, the enstrophy starts to rise once more. For the crest-to-trough collision without turbulence model, the enstrophy increases monotonically; the highest growth rate occur at the end of the calculation, where unphysical growth in kinetic energy is also experienced.

Kinetic energy spectra are also calculated for the four collision simulations. The spectra are also computed from the particle positions and strengths, as outlined in Appendix B. Energy spectra are shown in Fig. 16 for crest-to-crest collisions, and in Fig. 17 for crest-to-trough collisions. Curves are generated at times $t\,\Gamma/R^2 = 1.1$ (early stages of the simulation), 13.2 (during the stretching-induced enstrophy rise), 17.6 (the enstrophy plateau), and 22 or 24.2 (the end of the simulation). Features resolved by the particle filter fall in the

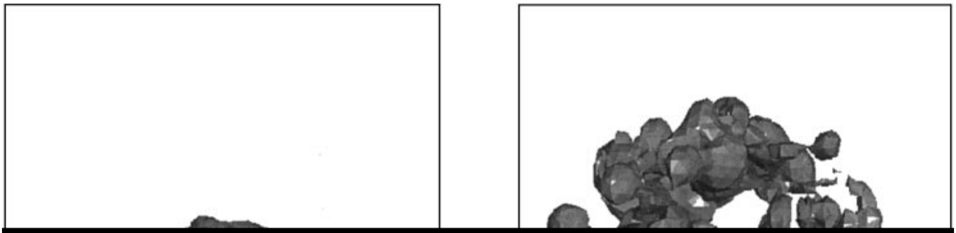

[redacted]

FIG. 10. Surface of constant vorticity magnitude ($\|\omega\| R^2/\Gamma = 1.82$) for crest-to-trough collision without turbulence model.

range $k\Delta < \pi$. A hump in the unresolved part of the spectrum is seen at early times which may be due to discretization of the vorticity field. For all simulations, low wavenumbers lose energy as time progresses, while the large wavenumbers gain in amplitude. For the present low Reynolds number calculations, no extended inertial range exists.

Energy spectra at the end of the simulation are shown together in Fig. 18 for all four collisions. The crest-to-trough collision without turbulence model, which resulted in a sharp, unphysical rise in kinetic energy at the end, exhibits more energy at all wavenumbers than the other three cases. The latter three have essentially the same shape, with the crest-to-crest collision without turbulence model having somewhat more energy than the two simulations with turbulence model.

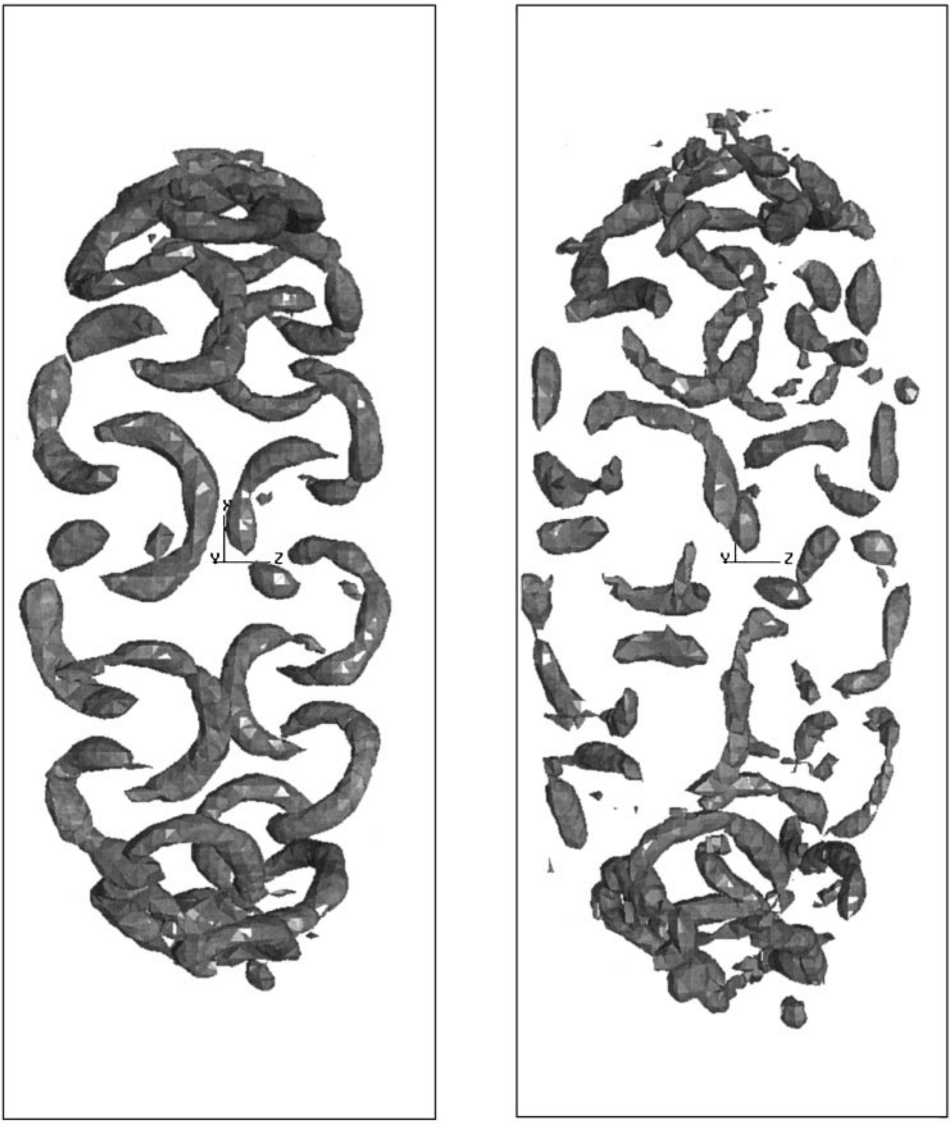

$t\Gamma/R^2 = 22$

$t\Gamma/R^2 = 24.2$

FIG. 11. Surface of constant vorticity magnitude ($\|\boldsymbol{\omega}\| R^2/\Gamma = 1.82$) for crest-to-trough collision with turbulence model.

4. SUMMARY AND DISCUSSION

In this work, a Lagrangian LES scheme is developed. The scheme combines an adaptive particle method with a simplified dynamic eddy diffusivity model. The particle scheme incorporates a local redistribution scheme which introduces new particles in regions of high strain and reduces the number of particles when the particles tend to cluster. The behavior of the scheme is examined in light of parallel computations of isolated vortex rings and collisions of two co-axial rings in three-dimensions. Based on these calculations, the following conclusions are reached:

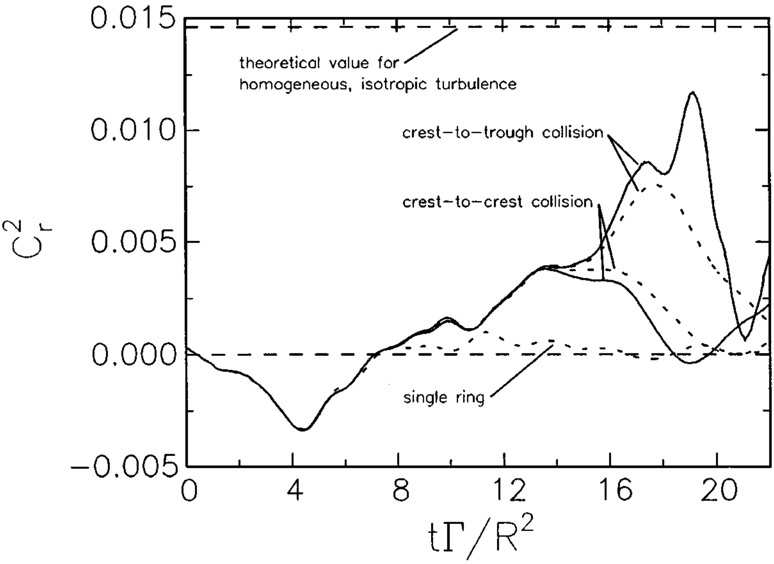

FIG. 12. Dynamic model coefficient. Solid lines are for simulations without turbulence model, and dashed lines are for simulations with turbulence model.

1. The behavior of the dynamic model coefficient is consistent with the flow behavior. The model coefficient has low magnitude in the initial stages of the computations, when the flow field is laminar, and only rises to appreciable levels when substantial spatial vorticity fluctuations develop.

2. For the conditions of the simulations, the turbulence model does not affect the propagation velocity or diameter expansion of the colliding rings prior to reconnection. Once reconnection starts, the dynamic model limits the rate of enstrophy growth.

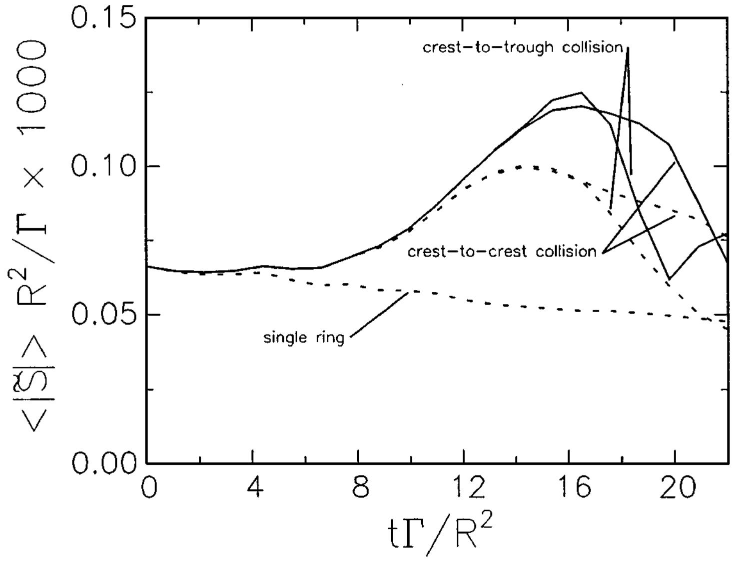

FIG. 13. Strain-rate modulus for simulations with (dashed) and without (solid) turbulence model.

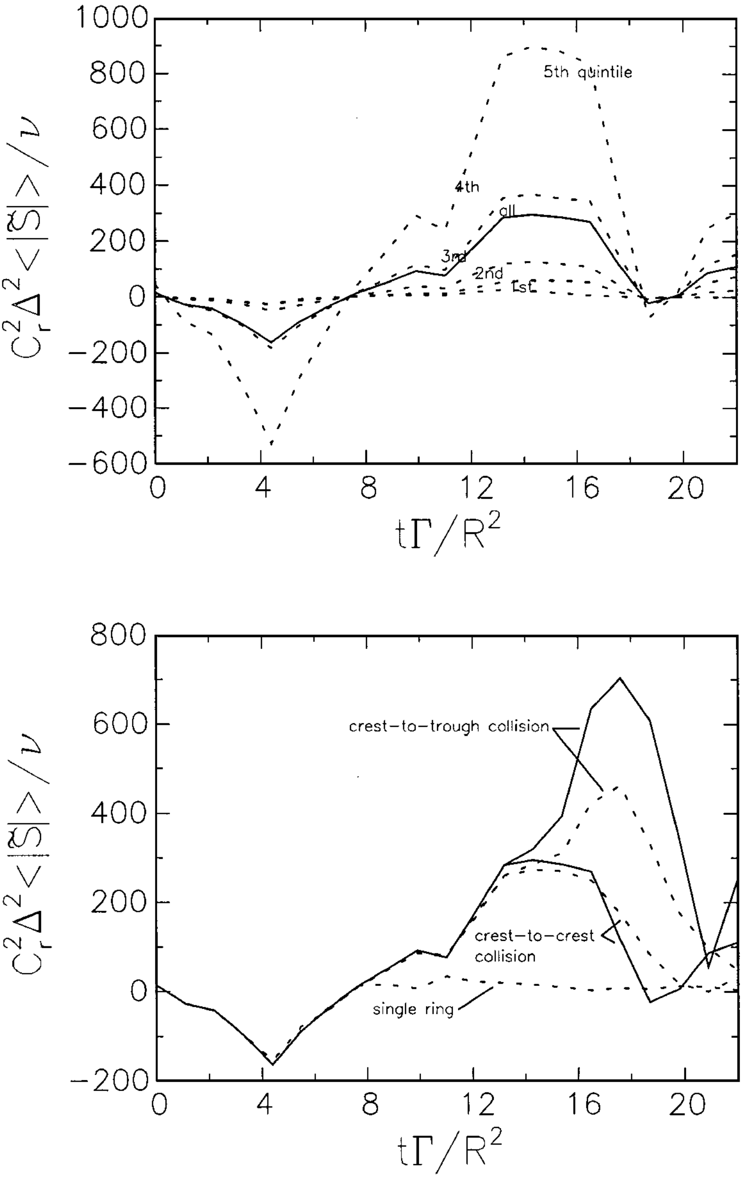

FIG. 14. Top: Eddy viscosity averaged over all vortex elements (solid line) and averaged over quintiles of the particles ranked by vorticity magnitude (dashed lines) for crest-to-crest collision without turbulence model. Bottom: Eddy viscosity for simulations with (dash) and without (solid) turbulence model.

3. The incorporation of dynamic SFS model and mesh redistribution scheme leads to a robust, adaptive Lagrangian particle scheme. This development enables us to extend the computations into the late stages of vortex ring collisions, where severe strain rates prevail. Earlier calculations [25] performed using a filament method without a scale removal scheme exhibited an explosive growth in the number of elements and were consequently restricted to the early stages of the collision event.

4. The computations of vortex ring collisions capture several distinctive phenomena that were observed in laboratory experiments [12], including the approach and stretching of

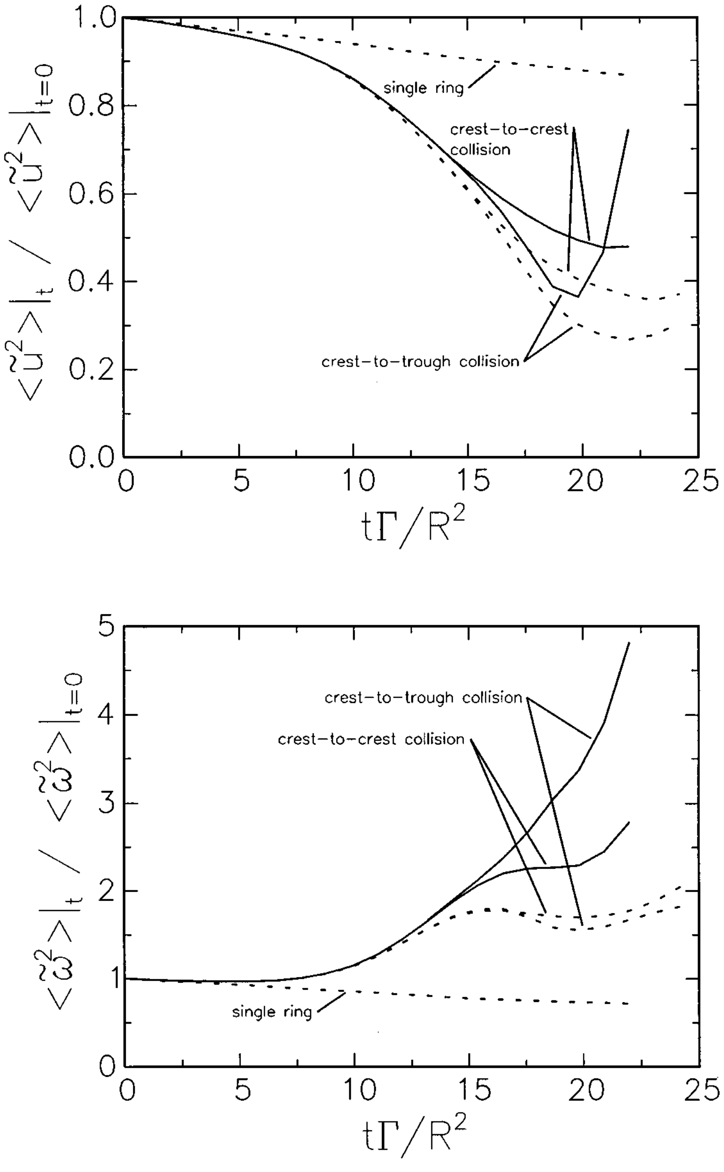

FIG. 15. Total normalized kinetic energy (top) and enstrophy (bottom). Solid lines are for simulations without turbulence model, and dashed lines are for simulations with turbulence model.

the rings, the development of three-dimensional azimuthal perturbations, strong interaction between the vortex cores with local cancellations and reconnections, the generation of small-scale turbulent structures, and the formation of ringlets propagating radially away from the center of collision. This indicates that numerical diffusion in the present computations is sufficiently low, despite the coarse resolution levels used. Note, however, that the ringlets leaving the collision are at the limits of the particle resolution used, and as a result appear to be blurred. This is typical of LES, in which structures frequently appear fatter (filtered) compared to the crisp appearance of the real structures that can be observed in dye visualization or in DNS.

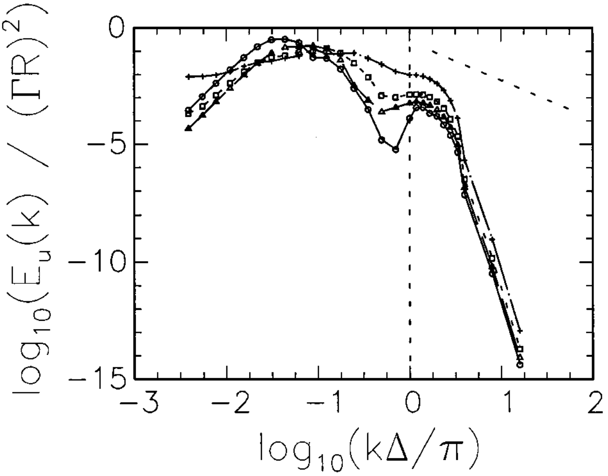

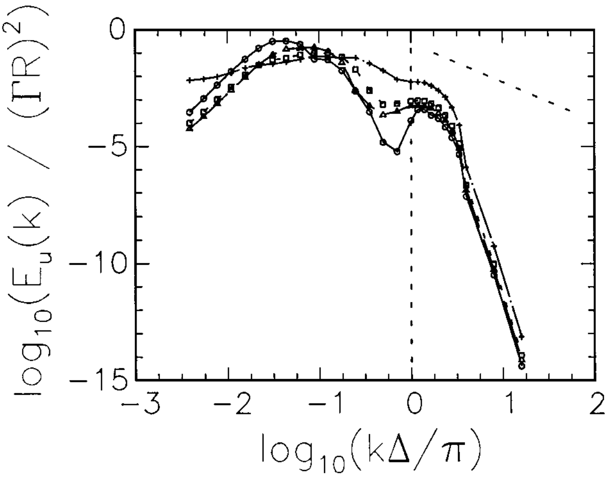

FIG. 16. Total energy spectra, crest-to-crest collisions. The top figure is the spectrum for the simulation without turbulence model and the bottom figure is for the simulation with model. Circles: $t\,\Gamma/R^2 = 1.1$, triangles: $t\,\Gamma/R^2 = 13.2$, squares: $t\,\Gamma/R^2 = 17.6$, crosses: $t\,\Gamma/R^2 = 22$ or 24.2. The dashed line in the upper-right corner shows a $-5/3$ slope.

5. The computations show that the outcome of the co-axial collision depends on the alignment of the initial azimuthal perturbation imposed on each of the rings. When a crest-to-crest alignment is imposed, the rings approach each other in such a way that their cores are locally nearly anti-parallel. This leads to a deformation which resembles the growth of the Crow instability [26] and, following cancellation and reconnection, to the generation of small-scale ringlets. On the other hand the crest-to-trough alignment results in a type of secondary flow instability which leads to a turbulent breakdown of the colliding rings. These two types of outcomes are consistent with and provide a plausible explanation for the experimental observations of Lim and Nickels [12].

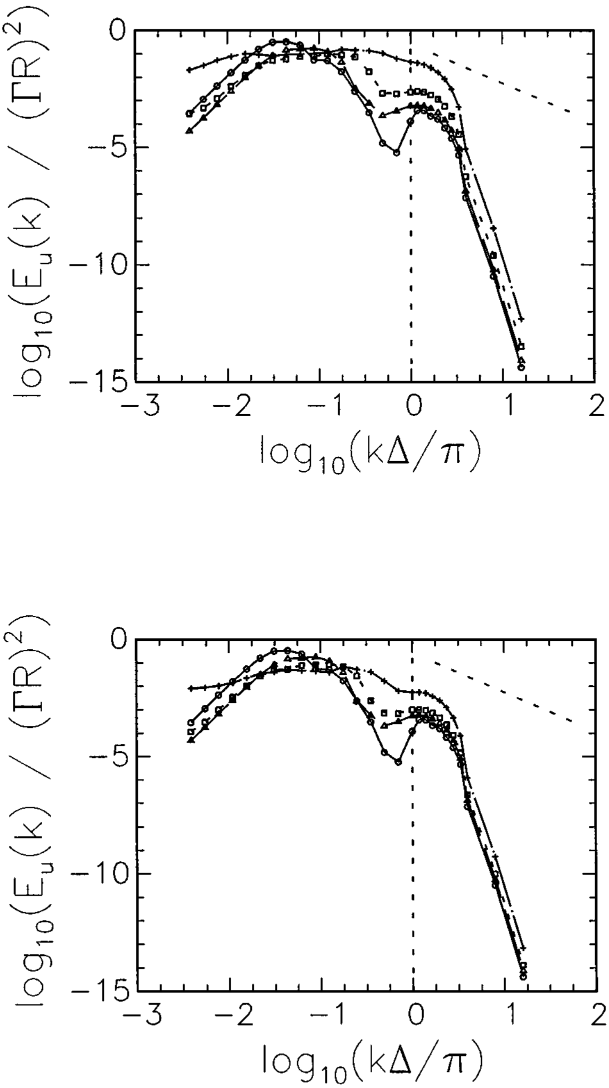

FIG. 17. Total energy spectra, crest-to-trough collisions. The top figure is the spectrum for the simulation without turbulence model and the bottom figure is for the simulation with model. Symbols: same as in Fig. 16.

Despite the advantages outlined above, the computations also indicate that the present model has some weaknesses which we plan to address in future efforts. One of these weaknesses concerns the simplified nature of the scale removal process, which is presently based on merging particles lying within a critical cutoff period. This approach is certainly less sophisticated than that of hairpin removal, which also involves the relative orientation of the vorticity vectors in the removal process [2]. Specifically, in hairpin removal only segments with nearly antiparallel vorticity are merged. On the other hand, in the present scheme merging of particles with closely aligned vorticity vectors is possible; in this case, merging would have an essentially anti-diffusive character. Extension of the merging scheme along the lines of hairpin removal [2] or filament surgery [6] appears to provide a suitable approach for improving this aspect of the particle computations.

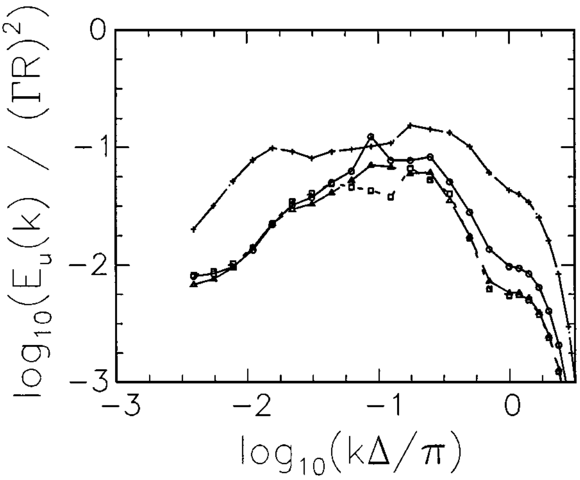

FIG. 18. Total energy spectra at end of simulations. Circles: crest-to-crest without model, triangles: crest-to-crest with model, crosses: crest-to-trough without model, squares: crest-to-trough with model. All four cases are compared at $t\Gamma/R^2 = 22$ for the simulations without turbulence model and $t\Gamma/R^2 = 24.2$ for the simulations with model. The slightly later time is selected for the simulations with model because the dissipation due to the model slightly slows the evolution of the rings.

Another area where additional work is needed is in clearly quantifying the effect of the SFS model, and distinguishing it from the effect of the removal scheme. To this end, one would need to extend the Lagrangian computations to model problems where the turbulence is well characterized, e.g. forced isotropic turbulence. An extension of the present Lagrangian scheme to accommodate such a setup is being explored.

Finally, in the present applications the dynamic coefficient is obtained by averaging over all the particles, thus combining information from very different regions of the flow (e.g. highly strained regions around vortex cores and "inactive" regions in the wakes) to determine a single coefficient in space. A conceptually more appealing method is to average in time following particle trajectories [27], an approach that is especially suited for Lagrangian methods. Extensions of the current scheme to incorporate such Lagrangian averaging should also be explored in future work.

APPENDIX A. EVALUATION OF ENSTROPHY AND KINETIC ENERGY

In this appendix we derive expressions for the total enstrophy and kinetic energy corresponding to a vorticity field given by the particle representation

$$\boldsymbol{\omega}^{\mathrm{N}}(\boldsymbol{x}) = \sum_{i=1}^{N} \zeta_i \, dV_i \, f_\delta(\boldsymbol{x} - \boldsymbol{X}_i). \tag{A-1}$$

A.1. *Enstrophy*

The total enstrophy, W, is defined by

$$W \equiv \iiint \frac{1}{2} |\boldsymbol{\omega}(\boldsymbol{x})|^2 \, d^3\boldsymbol{x}. \tag{A-2}$$

The total enstrophy corresponding to the vorticity field in (A-1) is thus given by

$$W = \frac{1}{2}\iiint\left(\sum_{i=1}^{N}\boldsymbol{\zeta}_i\,dV_i\,f_\delta(\boldsymbol{x}-\boldsymbol{X}_i)\right)^2 d^3\boldsymbol{x}$$

$$= \frac{1}{2}\sum_{i=1}^{N}\sum_{j=1}^{N}\{(\boldsymbol{\zeta}_i\cdot\boldsymbol{\zeta}_j)\,dV_i\,dV_j\,I(\boldsymbol{X}_i,\boldsymbol{X}_j)\}, \tag{A-3}$$

where

$$I(\boldsymbol{X}_i,\boldsymbol{X}_j) \equiv \iiint f_\delta(\boldsymbol{x}-\boldsymbol{X}_i)\,f_\delta(\boldsymbol{x}-\boldsymbol{X}_j)\,d^3\boldsymbol{x}. \tag{A-4}$$

Using a simple change of variables, I can be rewritten as

$$I(\boldsymbol{X}_i,\boldsymbol{X}_j) = \iiint f_\delta\left(\boldsymbol{x}-\frac{1}{2}r_{ij}\boldsymbol{e}\right) f_\delta\left(\boldsymbol{x}+\frac{1}{2}r_{ij}\boldsymbol{e}\right) d^3\boldsymbol{x}, \tag{A-5}$$

where $r_{ij} \equiv |\boldsymbol{X}_i - \boldsymbol{X}_j|$ is the distance between $\boldsymbol{X}_i$ and $\boldsymbol{X}_j$ and $\boldsymbol{e}$ is the unit vector in the direction of $\boldsymbol{X}_i - \boldsymbol{X}_j$, i.e., $\boldsymbol{e} = (\boldsymbol{X}_i - \boldsymbol{X}_j)/r_{ij}$. Since the core smoothing function f_δ is radially symmetric, I is independent of $\boldsymbol{e}$. Consequently, we can write

$$I(\boldsymbol{X}_i,\boldsymbol{X}_j) = g(|\boldsymbol{X}_i - \boldsymbol{X}_j|), \tag{A-6}$$

where

$$g(r) \equiv \iiint f_\delta\left(\boldsymbol{x}-\frac{1}{2}r\boldsymbol{e}\right) f_\delta\left(\boldsymbol{x}+\frac{1}{2}r\boldsymbol{e}\right) d^3\boldsymbol{x}. \tag{A-7}$$

Using the above definitions, the total enstrophy can be expressed as:

$$W = \frac{1}{2}g(0)\sum_{i=1}^{N}\left\{|\boldsymbol{\zeta}_i|^2\,dV_i^2\right\} + \sum_{i=1}^{N-1}\sum_{j=i+1}^{N}\{(\boldsymbol{\zeta}_i\cdot\boldsymbol{\zeta}_j)\,dV_i\,dV_j\,g(r_{ij})\}. \tag{A-8}$$

The core smoothing function f_δ used in this work is

$$f_\delta(\boldsymbol{x}) \equiv \frac{3}{4\pi\delta^3}\exp\left(-\frac{|\boldsymbol{x}|^3}{\delta^3}\right). \tag{A-9}$$

Choosing a cylindrical coordinate system to perform the integration, with axial direction aligned with $\boldsymbol{e}$, we have

$$g(r) = \frac{9}{16\pi^2\delta^3}\mathcal{I}(r^*), \tag{A-10}$$

where

$$r^* \equiv \frac{r}{2\delta} \tag{A-11}$$

and

$$\mathcal{I}(\xi) \equiv 2\pi \int_{-\infty}^{+\infty} \int_{0}^{\infty} \rho \exp[-((z-\xi)^2 + \rho^2)^{3/2} - ((z+\xi)^2 + \rho^2)^{3/2}]\, d\rho\, dz. \tag{A-12}$$

The kernel of the above integral decays quickly as $\xi \to \infty$, so that $\mathcal{I}$ can be accurately evaluated by numerical integration over a sufficiently large compact set. $\mathcal{I}(\xi)$ has Gaussian shape for $\xi < 1$. However, for $\xi > 1$, it falls noticeably below a true Gaussian. Thus, $\mathcal{I}$ is modeled as

$$\mathcal{I}(\xi) \approx \frac{2\pi}{3} \exp\left[-\left(\frac{\xi}{c(\xi)}\right)^2\right], \tag{A-13}$$

i.e., as a Gaussian with variable width, $c(\xi)$. A good fit for $c(\xi)$ is

$$c(\xi) = \begin{cases} 0.5944 & \xi \le 0.25 \\ 0.5944 + 0.0103(\xi - 0.25)^2 - 0.0812(\xi - 0.25)^3 & 0.25 < \xi < 1 \\ 0.5645 - 0.09406(\xi - 1) & 1 \le \xi \le 7 \\ 0.00014 & \xi > 7. \end{cases} \tag{A-14}$$

Using the above results and approximations, $g(r)$ is evaluated as

$$g(r) = \frac{3}{8\pi\delta^3} \exp\left[-\left(\frac{r^*}{c(r^*)}\right)^2\right]. \tag{A-15}$$

Finally, we have

$$W = \frac{3}{8\pi\delta^3}\left[\frac{1}{2}\sum_{i=1}^{N}\{|\zeta_i|^2\, dV_i^2\} + \sum_{i=1}^{N-1}\sum_{j=i+1}^{N}\left\{(\zeta_i \cdot \zeta_j)\, dV_i\, dV_j \exp\left[-\left(\frac{r_{ij}^*}{c(r_{ij}^*)}\right)^2\right]\right\}\right] \tag{A-16}$$

with c computed using Eq. (A-14).

A.2. *Kinetic energy*

Evaluation of the total kinetic energy, K, is more complicated than calculation of the total enstrophy because (a) expressions for K involve tensor manipulations, and (b) special attention is required for kernels with slow decay as $r \to \infty$.

The total kinetic energy associated with a given particle distribution is found by inserting the desingularized Biot–Savart law,

$$\boldsymbol{u}(\boldsymbol{x}) = -\frac{1}{4\pi}\sum_{i=1}^{N}\frac{(\boldsymbol{x} - \boldsymbol{X}_i) \times \boldsymbol{\zeta}_i}{|\boldsymbol{x} - \boldsymbol{X}_i|^3}\kappa_\delta(\boldsymbol{x} - \boldsymbol{X}_i), \tag{A-17}$$

into the definition of K,

$$K \equiv \iiint \frac{1}{2}|\boldsymbol{u}|^2\, d^3\boldsymbol{x}. \tag{A-18}$$

Expressing $\boldsymbol{u}$ and $\boldsymbol{\zeta}$ in component form, we have

$$K = \frac{1}{2}\frac{1}{(4\pi)^2}\sum_{i=1}^{N}\sum_{j=1}^{N}[\zeta_{p,i}\,dV_i\zeta_{p,j}\,dV_j J(\boldsymbol{X}_i, \boldsymbol{X}_j) - \zeta_{p,i}\,dV_i\zeta_{q,j}\,dV_j L_{pq}(\boldsymbol{X}_i, \boldsymbol{X}_j)], \tag{A-19}$$

where $k_\delta(\boldsymbol{x}) \equiv \kappa_\delta(\boldsymbol{x})/|\boldsymbol{x}|^3$,

$$J(\boldsymbol{X}_i, \boldsymbol{X}_j) \equiv \iiint (x_p - X_{p,i})(x_p - X_{p,j})k_\delta(\boldsymbol{x} - \boldsymbol{X}_i)k_\delta(\boldsymbol{x} - \boldsymbol{X}_j)\,d^3\boldsymbol{x} \tag{A-20}$$

$$L_{pq}(\boldsymbol{X}_i, \boldsymbol{X}_j) \equiv \iiint (x_p - X_{p,i})(x_q - X_{q,j})k_\delta(\boldsymbol{x} - \boldsymbol{X}_i)k_\delta(\boldsymbol{x} - \boldsymbol{X}_j)\,d^3\boldsymbol{x}. \tag{A-21}$$

$X_{p,i}$ denotes the p component of $\boldsymbol{X}_i$, $p = 1, 2, 3$ and $\zeta_{q,j}$ is the q component of $\boldsymbol{\zeta}_j$. Summation is understood whenever the indices p and q are repeated. Following the discussion above, J and L depend on the distance, r_{ij}, between $\boldsymbol{X}_i$ and $\boldsymbol{X}_j$ only. To highlight this dependence, we rewrite J and L as

$$J(\boldsymbol{X}_i, \boldsymbol{X}_j) = \iiint \left(x_p - \frac{r_{ij}}{2}e_p\right)\left(x_p + \frac{r_{ij}}{2}e_p\right)k_\delta\left(\boldsymbol{x} - \frac{r_{ij}}{2}\boldsymbol{e}\right)k_\delta\left(\boldsymbol{x} + \frac{r_{ij}}{2}\boldsymbol{e}\right)d^3\boldsymbol{x} \tag{A-22}$$

$$L_{pq}(\boldsymbol{X}_i, \boldsymbol{X}_j) = \iiint \left(x_p - \frac{r_{ij}}{2}e_p\right)\left(x_q + \frac{r_{ij}}{2}e_q\right)k_\delta\left(\boldsymbol{x} - \frac{r_{ij}}{2}\boldsymbol{e}\right)k_\delta\left(\boldsymbol{x} + \frac{r_{ij}}{2}\boldsymbol{e}\right)d^3\boldsymbol{x}, \tag{A-23}$$

where $\boldsymbol{e} \equiv (\boldsymbol{X}_i - \boldsymbol{X}_j)/r_{ij}$ as before.

Equation (A-19) can be simplified by manipulating the tensor expressions, and recasting the integrals in an appropriate cylindrical coordinate system. The velocity smoothing kernel corresponding to f is $\kappa(r) = 1 - \exp(-r^3)$ [15]. For this choice, we obtain

$$K = \frac{1}{2}\frac{1}{(4\pi)^2}h_\delta(0)\sum_{i=1}^{N}\left\{|\zeta_i|^2\,dV_i^2\right\} + \frac{1}{(4\pi)^2}\sum_{i=1}^{N-1}\sum_{j=i+1}^{N}\{(\boldsymbol{\zeta}_i \cdot \boldsymbol{\zeta}_j)\,dV_i\,dV_j h_\delta(r_{ij})\}, \tag{A-24}$$

where

$$h_\delta(r) \equiv \frac{1}{\delta}h\left(\frac{r}{2\delta}\right) \tag{A-25}$$

$$h(r) \equiv h_1(r) + h_2(r) \tag{A-26}$$

$$h_1(r) \equiv 2\pi\int_{-\infty}^{+\infty}\int_0^\infty \rho(\rho^2 + (z - r)(z + r))k_1(\rho, z)k_2(\rho, z)\,d\rho\,dz \tag{A-27}$$

$$h_2(r) \equiv 2\pi\int_{-\infty}^{+\infty}\int_0^\infty \rho(z - r)(z + r)k_1(\rho, z)k_2(\rho, z)\,d\rho\,dz \tag{A-28}$$

$$k_1(\rho, z) \equiv \frac{1 - \exp[-(\rho^2 + (z - r)^2)^{3/2}/\delta^3]}{(\rho^2 + (z - r)^2)^{3/2}} \tag{A-29}$$

$$k_2(\rho, z) \equiv \frac{1 - \exp[-(\rho^2 + (z + r)^2)^{3/2}/\delta^3]}{(\rho^2 + (z + r)^2)^{3/2}}. \tag{A-30}$$

(A-31)

Numerical integration is performed for h_1 and h_2 separately, and curve fits are made of those integrals as functions of r. The curve fits are combined to produce

$$h(r) \approx \begin{cases} A + Br^2 + Cr^3 + Dr^4 + Er^5 & 0 \le r \le 1.5 \\ \frac{2\pi}{r} - \frac{F}{r^3} & r > 1.5, \end{cases} \tag{A-32}$$

where $A = 8.395704$, $B = -5.629156$, $C = 2.334138$, $D = 0.623281$, $E = -0.375890$, and $F = 0.945098$. Consequently, the kinetic energy is computed using

$$K = \frac{1}{(4\pi)^2}\left[\frac{h_\delta(0)}{2}\sum_{i=1}^{N}\left\{|\zeta_i|^2\, dV_i^2\right\} + \sum_{i=1}^{N-1}\sum_{j=i+1}^{N}\{(\zeta_i\cdot\zeta_j)\, dV_i\, dV_j h_\delta(r_{ij})\}\right] \tag{A-33}$$

with h from Eq. (A-32).

APPENDIX B. ENERGY SPECTRUM

The radial energy spectrum is calculated directly from the particle distribution, following the procedure outlined below. We take advantage of the classical results for homogeneous flow where the velocity spectrum is simply the vorticity spectrum divided by k^2 [28], where k is the magnitude of the wavenumber vector $\boldsymbol{k}$, $k \equiv |\boldsymbol{k}|$. We begin by transforming the numerical vorticity distribution,

$$\boldsymbol{\omega}(\boldsymbol{x}) = \sum_{i=1}^{N}\zeta_i\, dV_i\, f_\delta(\boldsymbol{x} - \boldsymbol{X}_i), \tag{B-1}$$

to Fourier space; we have

$$\begin{aligned}\hat{\boldsymbol{\omega}}(\boldsymbol{k}) &\equiv \left(\frac{1}{2\pi}\right)^3 \iiint \boldsymbol{\omega}(\boldsymbol{x})\exp(-i\boldsymbol{k}\cdot\boldsymbol{x})\, d^3\boldsymbol{x} \\ &= \left(\frac{1}{2\pi}\right)^3 \sum_{i=1}^{N}\zeta_i\, dV_i \exp(-i\boldsymbol{k}\cdot\boldsymbol{X}_i)\iiint f_\delta(\boldsymbol{r})\exp(-i\boldsymbol{k}\cdot\boldsymbol{r})\, d^3\boldsymbol{r}.\end{aligned} \tag{B-2}$$

The conjugate of the vorticity amplitude is

$$\hat{\boldsymbol{\omega}}^*(\boldsymbol{k}) = \left(\frac{1}{2\pi}\right)^3 \sum_{j=1}^{N}\zeta_j\, dV_j \exp(+i\boldsymbol{k}\cdot\boldsymbol{X}_j)\iiint f_\delta(\boldsymbol{r})\exp(+i\boldsymbol{k}\cdot\boldsymbol{r})\, d^3\boldsymbol{r}. \tag{B-3}$$

Thus, the vorticity norm is given by

$$|\hat{\boldsymbol{\omega}}|^2(\boldsymbol{k}) = \left(\frac{1}{2\pi}\right)^6 R(\boldsymbol{k})S(\boldsymbol{k}), \tag{B-4}$$

where

$$R(\boldsymbol{k}) \equiv \iiint f_\delta(\boldsymbol{r})\exp(-i\boldsymbol{k}\cdot\boldsymbol{r})\, d^3\boldsymbol{r}\iiint f_\delta(\boldsymbol{r})\exp(+i\boldsymbol{k}\cdot\boldsymbol{r})\, d^3\boldsymbol{r} \tag{B-5}$$

and

$$S(k) \equiv \sum_{i=1}^{N} \sum_{j=1}^{N} (\alpha_i \cdot \alpha_j)\, dV_i\, dV_j \exp[-i\,k \cdot (X_i - X_j)]. \tag{B-6}$$

R simplifies to

$$R(k) = \left[\frac{4\pi}{\sigma^3} \int_0^\infty r^2 f(r) \frac{\sin(kr)}{kr}\, dr \right]^2, \tag{B-7}$$

where f is the "normalized" core smoothing function [15]. Consequently, R depends on the magnitude, k, of the wavenumber vector but not its orientation. For $f = (3/4\pi)\exp(-r^3)$, we have

$$R(k) = \left[3 \int_0^\infty \rho^2 \exp(-\rho^3) \frac{\sin(k\Delta\rho/2.88)}{k\Delta\rho/2.88}\, d\rho \right]^2, \tag{B-8}$$

where $\Delta = 2.88\sigma$ is the ("normalized") filter size [10]. Values of R for a suitable range of $k\Delta$ are obtained by numerical evaluation of the integral in the above equation. The origi expression for S is also simplified and expressed as

$$S(k) = \sum_{i=1}^{N} |\alpha_i|^2 dV_i^2 + \sum_{i=1}^{N-1} \sum_{j=i+1}^{N} \{(\alpha_i \cdot \alpha_j)\, dV_i\, dV_j \times 2\cos[k \cdot (X_i - X_j)]\}. \tag{B-9}$$

The 3D radial vorticity spectrum is defined by (spherical) integration over shells constant k; specifically,

$$\begin{aligned} E_\omega(k) &\equiv (2\pi)^3 \int_0^{2\pi} \int_0^{\pi} \hat{\omega}(k) \cdot \hat{\omega}^*(k)\, k^2 \sin\theta\, d\theta\, d\phi \\ &= \left(\frac{1}{2\pi}\right)^2 k^2 R(k) \sum_{i=1}^{N} \sum_{j=1}^{N} (\alpha_i \cdot \alpha_j)\, dV_i\, dV_j \frac{\sin(k|X_i - X_j|)}{k|X_i - X_j|}. \end{aligned} \tag{B-10}$$

Finally, the radial energy spectrum, $E_u(k)$, is evaluated according to $E_u(k) = E_\omega(k)/k^2$; we have

$$E_u(k) = \left(\frac{1}{2\pi}\right)^2 R(k) \sum_{i=1}^{N} \sum_{j=1}^{N} (\alpha_i \cdot \alpha_j)\, dV_i\, dV_j \frac{\sin(k|X_i - X_j|)}{k|X_i - X_j|}. \tag{B-11}$$

This expression agrees with the result of Winckelmans [29], except that $R(k)$ is here given by Eq. (B-8) for the third-order exponential core function instead of a regular Gaussian

ACKNOWLEDGMENTS

This work was supported in part by the National Science Foundation through Grants ECS-9424432 and C 9408344 and by the Office of Naval Research through Grant N00014-97-10429. Computer resources were pro through NSF Equipment Grant CTS-9506077 and by the Pittsburgh Supercomputer Center under NSF Grant C 930041P. OK also acknowledges helpful discussions with Professor A. Chorin.

REFERENCES

1. A. J. Chorin, Hairpin removal in vortex interactions, *J. Comput. Phy.* **91**, 1 (1990).
2. A. J. Chorin, Hairpin removal in vortex interactions, II, *J. Comput. Phy.* **107**, 1 (1993).
3. A. Chorin, *Vorticity and Turbulence*, Springer-Verlag, Berlin/New York, 1993.
4. P. S. Bernard, A vortex method for wall bounded turbulent flows, *ESAIM Proc.* **1**, 15 (1996).
5. J.-C. Saghbini, *Simulation of Vorticity Dynamics in Swirling Flows, Mixing and Vortex Breakdown*, M.Sc. thesis, Department of Mechanical Engineering, Massachusetts Institute of Technology, 1996.
6. V. M. Fernandez, N. J. Zabusky, P. Liu, S. Bhatt, and A. Gerasoulis, Filament surgery and temporal grid adaptivity extensions to a parallel tree code for simulation and diagnosis in 3D vortex dynamics, *ESAIM Proc.* **1**, 197 (1996).
7. A. J. Chorin and O. H. Hald, Vortex renormalization in 3 space dimensions, *Phys. Rev. B* **51**, 11,969 (1995).
8. A. J. Chorin, Microstructure, renormalization, and more efficient vortex methods, *ESAIM Proc.* **1**, 1 (1996).
9. A. J. Chorin and O. H. Hald, Analysis of Kosterlitz–Thouless transition models, *Physica D* **99**, 442 (1997).
10. J. R. Mansfield, O. M. Knio, and C. Meneveau, A dynamic LES scheme for the vorticity transport equation: Formulation and a priori tests, *J. Comput. Phys.* **145**, 693 (1998).
11. G. S. Winckelmans, T. S. Lund, D. Carati, and A. A. Wray, A priori testing of subgrid-scale models for the velocity–pressure and velocity–vorticity formulations, in *Center of Turbulence Research Proceedings of the Summer Program*, 1996, p. 309.
12. T. T. Lim and T. B. Nickels, Instability and reconnection in the head-on collision of two vortex rings, *Nature* **357**, 225 (1992).
13. J. R. Mansfield, O. M. Knio, and C. Meneveau, Towards large vortex simulation, *ESAIM Proc.* **1**, 49 (1996).
14. O. H. Hald, Convergence of vortex methods for Euler's equations, II, *SIAM J. Numer. Anal.* **16**, 726 (1979).
15. J. T. Beale and A. Majda, High order accurate vortex method with explicit velocity kernels, *J. Comput. Phys.* **58**, 188 (1985).
16. J. T. Beale, A convergent 3-D vortex method with grid-free stretching, *Math. Comput.* **46**, 401 (1986).
17. A. Leonard, Vortex methods for flow simulation, *J. Comput. Phys.* **37**, 289 (1980).
18. M. Germano, U. Piomelli, P. Moin, and W. H. Cabot, A dynamic subgrid-scale eddy viscosity model, *Phys. Fluids A* **3**, 1760 (1991).
19. J. R. Mansfield, *A Dynamic Lagrangian LES Scheme for the Vorticity Transport Equation*, Ph.D. thesis, Johns Hopkins University, 1997.
20. P. Degond and S. Mas-Gallic, The weighted particle method for convection–diffusion equations, I. The case of an isotropic viscosity, II. The anisotropic case, *Math. Comput.* **53**, 485 (1989).
21. O. M. Knio and A. F. Ghoniem, Three-dimensional vortex simulation of rollup and entrainment in a shear layer, *J. Comput. Phys.* **97**, 172 (1991).
22. O. M. Knio and A. F. Ghoniem, Numerical study of a three-dimensional vortex method, *J. Comput. Phys.* **86**, 75 (1990).
23. F. Hauville, C. Bertelle, S. Huberson, and O. M. Knio, Application of particle methods on parallel architectures, preprint (1998).
24. S. E. Widnall and C.-Y. Tsai, The instability of the thin ring of constant vorticity, *Proc. R. Soc. London A* **287**, 273 (1977).
25. O. Knio and D. Juvé, On noise emission during coaxial vortex ring collision, *C. R. Acad. Sci. Paris Ser. II* **322**, 591 (1996).
26. S. C. Crow, Stability theory for a pair of trailing vortices, *AIAA J.* **8**, 2172 (1970).
27. C. Meneveau, T. Lund, and W. Cabot, A lagrangian dynamic subgrid-scale model of turbulence, *J. Fluid Mech.* **319**, 353 (1996).
28. G. K. Batchelor, *The Theory of Homogeneous Turbulence*, Cambridge Univ. Press, Cambridge, UK, 1953.
29. G. S. Winckelmans, Some progress in large-eddy simulation using the 3-d vortex particle method, in *Center for Turbulence Research Annual Research Briefs*, 1995, p. 391.